

## Article

# Numerical Simulation of Hydrate Decomposition during the Drilling Process of the Hydrate Reservoir in the Northern South China Sea

Lei Zhang <sup>1,2,3</sup>, Yu Zhang <sup>1,2,3,\*</sup>, Chang Chen <sup>1,2,3</sup>, Xiao-Sen Li <sup>1,2,3,\*</sup> and Zhao-Yang Chen <sup>1,2,3</sup> 

- <sup>1</sup> Key Laboratory of Gas Hydrate, Guangzhou Institute of Energy Conversion, Chinese Academy of Sciences, Guangzhou 510640, China; zhanglei@ms.giec.ac.cn (L.Z.); chenchang@ms.giec.ac.cn (C.C.); chenzy@ms.giec.ac.cn (Z.-Y.C.)
- <sup>2</sup> Guangdong Provincial Key Laboratory of New and Renewable Energy Research and Development, Guangzhou 510640, China
- <sup>3</sup> University of Chinese Academy of Sciences, Beijing 100083, China
- \* Correspondence: zhangyu1@ms.giec.ac.cn (Y.Z.); lixs@ms.giec.ac.cn (X.-S.L.); Tel.: +86-20-8705-8054 (Y.Z.); +86-20-8705-7037 (X.-S.L.)

**Abstract:** The process of drilling in natural gas hydrate reservoirs in sea areas involves problems such as hydrate decomposition and wellbore instability. To study the response behaviors of a reservoir during the drilling process, a two-dimensional numerical model of drilling fluid invading a hydrate reservoir in a cylindrical coordinate system was established to simulate the processes of heat and mass transfer, gas–liquid two-phase flow, and hydrate formation and decomposition in the hydrate reservoir during the drilling process. Based on the hydrate reservoir at station W17, Shenhu area of the South China Sea, the physical property response of the hydrate reservoir under different drilling fluid temperatures and salinity values was studied. The simulation results showed that during the drilling process, the temperature and pressure of the reservoir respond rapidly in a large area, further promoting the hydrate decomposition in the reservoir around the wellbore and leading to secondary hydrate formation. Moreover, a high hydrate saturation zone appears near the decomposed hydrate area in the layer without free gas, which corresponds to the low water saturation and high salinity zone. The hydrate decomposition area in the layer with free gas is larger than that without free gas. The increase in the drilling fluid temperature significantly enhances the hydrate decomposition in both layers of the reservoir. The hydrate decomposition near the wellbore under the high drilling fluid temperature will cause a sharp increase in the pressure in the reservoir, leading to the flow of pore fluid into the wellbore. The increase in drilling fluid salinity has little effect on the range of the hydrate decomposition in the reservoir but significantly increases the salinity of the pore water in the layer with free gas. As the drilling fluid temperature increases, the possibility of the gas invasion from the reservoir into the wellbore will be greatly increased at the early stage.

**Keywords:** drilling process; hydrate decomposition; secondary hydrate formation; drilling fluid temperature; salinity



**Citation:** Zhang, L.; Zhang, Y.; Chen, C.; Li, X.-S.; Chen, Z.-Y. Numerical Simulation of Hydrate Decomposition during the Drilling Process of the Hydrate Reservoir in the Northern South China Sea. *Energies* **2022**, *15*, 3273. <https://doi.org/10.3390/en15093273>

Academic Editor: Reza Rezaee

Received: 19 March 2022

Accepted: 26 April 2022

Published: 29 April 2022

**Publisher's Note:** MDPI stays neutral with regard to jurisdictional claims in published maps and institutional affiliations.



**Copyright:** © 2022 by the authors. Licensee MDPI, Basel, Switzerland. This article is an open access article distributed under the terms and conditions of the Creative Commons Attribution (CC BY) license (<https://creativecommons.org/licenses/by/4.0/>).

## 1. Introduction

With the increasing depletion of fossil energy, alternative energy sources such as natural gas hydrate and deep geothermal energy have received extensive attention from countries all over the world [1,2]. Natural gas hydrate is distributed globally in the shallow layer of the sea strata and terrestrial permafrost regions [3], and its reserve accounts for more than 50% of all the carbon-containing fuel reserves on the earth [4]. Due to various influencing factors such as geological structure, sedimentation, geothermal gradient, and other factors, the majority of natural gas hydrate reservoirs are distributed in the seabed sediments near the ocean coast [5].

Natural gas hydrate reservoirs are usually located in the deep seabed with water depth exceeding several hundred meters [6] and are affected by complex marine environmental factors such as submarine landslide, density current, faulting, submarine leakage, and submarine current scouring [7]. The hydrate reservoirs are mostly permeable semi-consolidated or unconsolidated sandstone or argillaceous sandstone strata [8]. Therefore, a hydrate reservoir usually has a low cementation strength of the sediments, and the drilling environment in hydrate reservoirs is harsh. At present, many countries have successively carried out drilling exploration of natural gas hydrate reservoirs [9]. However, about 70% of these explorations were affected by the decomposition of natural gas hydrate [10]. During the drilling in a hydrate reservoir, it is necessary to reduce the decomposition of natural gas hydrate in the reservoir to maintain the stability of the reservoir and avoid secondary hydrate formation in the wellbore. Up to now, the technologies for drilling in hydrate reservoirs are still in their infancy, and the risk of drilling in these reservoirs is higher than that of traditional oil and gas reservoirs.

The drilling process can affect the stratigraphic structure, leading to the stress release of the hydrate reservoir around the wellbore and affecting the stability of the hydrate reservoir [11]. Therefore, to maintain the mechanical stability of the hydrate reservoir around the wellbore, the drilling fluid pressure in the wellbore is commonly kept higher than that of the hydrate reservoir during the drilling process [12], resulting in the drilling fluid displacing the original pore fluid around the wellbore and invading the hydrate reservoir due to the pressure differential. The invasion of the drilling fluid is accompanied by the heat transfer between the drilling fluid and the hydrate reservoir. Therefore, the invasion of the drilling fluid may make the pressure, temperature, and salinity of the hydrate reservoir deviate from the equilibrium state, resulting in the hydrate decomposition and production of a large amount of water and natural gas. Additionally, this can change the physical characteristics of the hydrate reservoir and reduce the mechanical strength, as well as promoting the instability or collapse of the hydrate reservoir. A large amount of methane gas generated by hydrate decomposition also may enter the drilling fluid and pipeline in the wellbore, which promotes hydrate formation with local water under the proper pressure and temperature [13], resulting in the degradation of the drilling fluid performance [14], pipeline blockage [15], and other problems. In severe cases, it can cause drilling stagnation and equipment damage [16]. Therefore, it is of great importance to study and analyze the physical response characteristics of a natural gas hydrate reservoir during the drilling process and determine the appropriate parameters of the drilling fluid.

Numerous reports have studied the process of drilling fluid invasion into hydrate reservoirs by numerical simulation, including the heat and mass transfer between the reservoir and wellbore, hydrate decomposition characteristics, and changes in the mechanical properties of the reservoir. Gao et al. [17] established a model of heat transfer between the wellbore and the hydrate reservoir during the drilling process. The temperature distribution of the hydrate reservoir under various drilling fluid temperatures, flow rates, and circulation times was simulated. The authors analyzed the possible hydrate decomposition area in the hydrate reservoir by combining experimental results. It was found that excessive circulation rate and time of the drilling fluid can influence hydrate decomposition. Reem Freij-Ayoub et al. [18] established a wellbore stability model for hydrate reservoirs during the drilling process that couples the thermodynamic stability of hydrates, fluid heat transfer, and mechanical deformation of hydrate reservoirs. The drilling process of the reservoir in the Gulf of Mexico was simulated. It was found that the increase in drilling fluid temperature and density can cause instability of the hydrate and lead to an increase in the reservoir pressure. A mathematical model integrating the hydrate decomposition and heat transfer between the wellbore and hydrate reservoir and its influence on mechanical properties was established by Cheng et al. [19]. The simulation of the drilling fluid invasion into the hydrate reservoir in the Gulf of Mexico revealed that the increasing temperature aggravates the decomposition of methane hydrate around the wellbore. Ning et al. [12] simplified the invasion process of the drilling fluid as a one-dimensional planar multiphase flow displace-

ment problem and simulated the drilling fluid invasion into the hydrate reservoir in the Gulf of Mexico using Tough + Hydrate software. The results indicated that temperature, density, and drilling fluid salinity have varying degrees of influence on the decomposition and secondary formation of the hydrate. The secondary formation of hydrate is controlled by drilling fluid salinity and temperature, leading to the formation of a high apparent resistivity zone around the wellbore and distorting the logging results. Sun et al. [20] established a model considering the gas–liquid flow, heat transfer, and changes in the mechanical properties during drilling fluid invasion into a hydrate reservoir. The effects of the temperature, salinity, density, and initial reservoir conditions on the stability of the hydrate reservoir were studied based on the first exploration well of the hydrate reservoir in the Shenhu sea area of China South Sea in 2007. The results showed that an increase in the thermal field around the wellbore and changes in water salinity are the main factors affecting the hydrate dissociation, which may lead to a larger excess of the pore pressure and trigger wellbore instability issues. Li et al. [21] established a coupling mathematical model considering the fluid seepage, heat transfer, methane hydrate decomposition, and wellbore deformation process; the model mainly focused on the influence of the drilling fluid density on the hydrate decomposition and wellbore stability and ignored the influence of the temperature and salinity of the drilling fluid. The results showed that the influence of the drilling fluid pressure on the invasion process is considerably greater than that of the drilling fluid temperature, and the increase in the drilling fluid density is beneficial for inhibiting the decomposition of the hydrate near the wellbore. Zhang et al. [10] reported a mathematical model of multifield coupling between wellbores and hydrate reservoirs by considering hydrate decomposition and transformation of the formation framework in the hydrate reservoir of the Liwan slope in the northern part of the South China Sea. The influences of the temperature, density, and soaking time of the drilling fluid on the stability of hydrate reservoirs were analyzed. The results showed that the larger the temperature difference of heat transfer is in the invasion process, the more hydrate is decomposed in the reservoir, and a reduction in soaking time benefits the wellbore stability of hydrate reservoirs. Lu et al. [22] established a two-dimensional numerical model to study the hydrate decomposition and gas flowing into a wellbore during the drilling process. It indicated that small-to-moderate gas invasion occurs during the drilling process of a hydrate reservoir. Huang et al. [23] built a one-dimensional cylindrical numerical model to simulate the drilling fluid invasion process in the reservoir of the Shenhu sea area. The effect of the reservoir's permeability on the drilling fluid invasion process was studied. It was found that the extent of hydrate decomposition and drilling fluid invasion depth increase with the increase in the lateral permeability of the hydrate reservoir.

To the best of our knowledge, the heat and mass transfer between the wellbore and reservoir during the drilling process may cause massive hydrate decomposition around the wellbore, and the characteristics of the drilling fluid have a significant influence on the heat and mass transfer and hydrate decomposition in a hydrate reservoir. In actual hydrate reservoirs, the stratum has obvious temperature and pressure gradient distributions in the vertical direction, and natural gas hydrates of varying depths are in different stable states. Therefore, the physical response of the hydrate reservoir at different depths during the drilling process is different. In addition, the flow of water and gas under the action of gravity has a certain influence on the distributions of water and gas in the reservoir. The complex distributions of the hydrate, water, and free gas in the reservoir significantly affect the changes in the temperature and pressure in the reservoir during the drilling process. According to the classification of natural gas hydrate reservoirs proposed by Moridis et al. [24], the first type of reservoir, which contains free gas, water, and hydrate at the bottom of the reservoir, is the most favorable for exploitation. At station W17 of the hydrate reservoir in the Shenhu area of the South China Sea, there are two different hydrate reservoir types: one only contains natural gas hydrate and water, and the other contains a small amount of methane gas at the bottom of the reservoir [25]. The physical property responses of various reservoir types during the drilling process are different.

However, research conducted on drilling fluid invasion into a hydrate reservoir containing free methane gas is relatively lacking. Most of the established numerical models are aimed at reservoirs containing water without free gas. Additionally, the effect of free gas on the decomposition and formation of hydrate during the drilling process is neglected.

In this study, a numerical model for the drilling process of marine hydrate reservoirs based on a two-dimensional cylindrical coordinate system was established, considering the heat and mass transfer processes of multiphase fluid in the hydrate layer, Darcy seepage process, hydrate decomposition, and formation kinetics. Station W17 in the Shenhu area of the South China Sea has complex hydrate reservoir physical conditions. The behavior of secondary hydrate formation, invasion amount of the drilling fluid, gas production from the hydrate decomposition, and salinity distribution in the reservoir around the wellbore were simulated based on the hydrate reservoir physical conditions. The drilling fluid salinity and temperature are the most important and controllable parameters for maintaining reservoir stability and preventing pipeline blockage in the wellbore. Therefore, their effects on the multiphase saturation distribution and the heat and mass transfer process of the reservoir during the drilling process were investigated. The influence of the presence of free gas on the corresponding characteristics of the reservoir during drilling was analyzed. This study can provide a basis for the formulation of drilling plans for hydrate reservoirs in marine target areas and the analysis of logging results.

## 2. Numerical Models

In this study, a mathematical model of the drilling process of marine gas hydrate reservoirs under the two-dimensional cylindrical coordinate system is established. The model considers the radial displacement process of the drilling process and the change in the vertical physical property of the hydrate reservoir. The model contains hydrate decomposition kinetics, gas–liquid two-phase flow, heat and mass transfer processes of the hydrate layer, etc. In order to solve the model by finite difference, the following assumptions are proposed:

- (1) Only considering the gas–liquid flow in hydrate reservoirs, the solid phase cannot flow, and Darcy's law is effective.
- (2) The rock–soil framework of methane hydrate and hydrate reservoirs is incompressible.
- (3) The mud layer formed on the borehole wall is thin, and its distribution is uneven and discontinuous. Therefore, the influence of the mud layer on the invasion of drilling fluid into the hydrate reservoirs is ignored.
- (4) The radiation heat transfer and the throttling effect in the heat transfer are ignored.
- (5) It is assumed that the cracks and voids in the hydrate reservoirs around the wellbore are evenly distributed, and every phase in the reservoirs is even.
- (6) Only the injection pressure and outflow pressure of drilling fluid are considered, ignoring the friction of cement slurry on the casing and borehole wall.
- (7) The decomposition of methane hydrate is considered as a continuous water–gas source term with varying intensity.
- (8) The dissolution of gas generated by methane hydrate decomposition in the water is ignored.
- (9) The change in drilling depth with time during the drilling process is not considered.

### 2.1. Model of the Mass Transfer Process in the Hydrate Reservoir

#### 2.1.1. Mass Conservation Equation of Gas, Liquid, Hydrate, and Salinity

Mass conservation equation of gas phase:

$$\frac{\partial(\varphi\rho_g S_g)}{\partial t} = -\frac{1}{r} \frac{\partial}{\partial r}(r\rho_g v_{gr}) - \frac{\partial}{\partial z}(\rho_g v_{gz}) + \dot{m}_g M_g \quad (1)$$

Mass conservation equation of liquid phase:

$$\frac{\partial(\varphi\rho_w S_w)}{\partial t} = -\frac{1}{r} \frac{\partial}{\partial r}(r\rho_w v_{wr}) - \frac{\partial}{\partial z}(\rho_w v_{wz}) + m_w M_w \quad (2)$$

Mass conservation equation of void water salinity:

$$\frac{\partial(\varphi\rho_w S_w X_s)}{\partial t} = -\frac{1}{r} \frac{\partial}{\partial r}(r\rho_w X_s v_{wr}) - \frac{\partial}{\partial z}(\rho_w X_s v_{wz}) + k_D \left\{ \frac{1}{r} \frac{\partial}{\partial r}(\varphi r \rho_w S_w \frac{\partial X_s}{\partial r}) + \frac{\partial}{\partial z}(\varphi \rho_w S_w \frac{\partial X_s}{\partial z}) \right\} \quad (3)$$

Mass conservation equation of hydrate phase:

$$\varphi\rho_h \frac{\partial(S_h)}{\partial t} = -m_h(M_g + n_w M_w) \quad (4)$$

where  $t$  is the calculation time, s;  $r$  is the radial dimension of the model, m;  $z$  is the vertical dimension of the model, m;  $\varphi$  is the porosity of the hydrate reservoir;  $P_w$  and  $P_g$  are the water pressure and gas pressure, MPa;  $\rho_r$ ,  $\rho_w$ ,  $\rho_g$ , and  $\rho_h$  are the mass densities of rock–soil skeleton, water, gas, and hydrate, kg/m<sup>3</sup>;  $S_w$ ,  $S_g$ , and  $S_h$  are the saturation of water, gas, and hydrate;  $X_s$  is the salinity;  $M_g$  and  $M_w$  are the molar masses of gas and water, kg/mol;  $m_g$ ,  $m_w$ , and  $m_h$  are the molar source terms of gas, water, and hydrate, mol/(m<sup>3</sup>·s);  $n_w$  is the hydrate number;  $v_{gr}$  is the seepage velocity of methane gas along the  $r$  direction, m/s;  $v_{gz}$  is the seepage velocity of methane gas along the  $z$  direction, m/s;  $v_{wr}$  is the seepage velocity of liquid along the  $r$  direction, m/s; and  $v_{wz}$  is the seepage velocity of liquid along the  $z$  direction, m/s.

In the equations,  $m_g$ ,  $m_w$ , and  $m_h$  originate from the decomposition and formation of natural gas hydrate during the drilling process and are calculated according to the hydrate decomposition kinetic model of Kim et al. [26] and the hydrate formation equation built by Malegaonka et al. [27].

### 2.1.2. Darcy's Law Seepage Velocity Equation

Because the methane hydrate in reservoirs is in a solid state and cannot flow, only the methane gas and water can flow through the porous medium of hydrate reservoirs. It can be assumed that the flow of methane gas and water follows Darcy's law. Finally, the seepage velocity of methane gas and water in porous media in all considered directions can be calculated.

Seepage velocity of methane gas along the  $r$  direction:

$$v_{gr} = -\frac{KK_g}{\mu_g} \frac{\partial P_g}{\partial r} \quad (5)$$

Seepage velocity of methane gas along the  $z$  direction:

$$v_{gz} = -\frac{KK_g}{\mu_g} \frac{\partial (P_g - \gamma_{gz} g \Delta z)}{\partial z} \quad (6)$$

Seepage velocity of void water along the  $r$  direction:

$$v_{wr} = -\frac{KK_w}{\mu_w} \frac{\partial P_w}{\partial r} \quad (7)$$

Seepage velocity of void water along the  $z$  direction:

$$v_{wz} = -\frac{KK_w}{\mu_w} \frac{\partial (P_w - \gamma_{wz} g \Delta z)}{\partial z} \quad (8)$$

where  $K$  is the radial absolute permeability of hydrate reservoir, mD;  $K_w$  and  $K_g$  are the relative permeabilities of water and methane gas;  $\mu_g$  and  $\mu_w$  are the dynamic viscosities of gas and water, and they are constant in this model, MPa·s;  $g$  is the acceleration of gravity,

$m/s^2$ ;  $\gamma_{wz}$  is the specific gravity of water,  $kg/m^3$ ;  $\gamma_{gz}$  is the specific gravity of methane gas,  $kg/m^3$ ; and  $\Delta z$  is the height difference between the different layers of the reservoir,  $m$ .

In the equations,  $K$  is calculated according to the permeability model proposed by Masuda et al. [28];  $K_w$  and  $K_g$  are calculated according to the relative permeability equation of Stone [29].

## 2.2. Model of the Heat Transfer Process in the Hydrate Reservoir

In the invasion process of drilling fluid, the energy transfer process of the hydrate reservoir includes heat conduction, heat convection, energy injection and outflow, and the endothermic process of methane hydrate decomposition involving phase change. Therefore, in this model, the energy conservation equation is expressed by temperature and enthalpy changes of components, as follows:

$$\frac{1}{r} \frac{\partial}{\partial r} (r \lambda_c \frac{\partial T}{\partial r}) + \frac{\partial}{\partial z} (\lambda_c \frac{\partial T}{\partial z}) - \frac{\partial}{\partial r} \{r(\rho_g C_g T v_{gr} + \rho_w C_w T v_{wr})\} - \frac{\partial}{\partial z} (\rho_g C_g T v_{gz} + \rho_w C_w T v_{wz}) - \dot{m}_h \Delta H = \frac{\partial(TC_t)}{\partial t} \quad (9)$$

$$C_t = (1 - \varphi) \rho_r C_r + \varphi (S_h \rho_h C_h + S_w \rho_w C_w + S_g \rho_g C_g) \quad (10)$$

$$\lambda_c = 1 - \varphi \lambda_r + \varphi (S_w \lambda_w + S_g \lambda_g + S_h \lambda_h) \quad (11)$$

where  $T$  is the temperature,  $K$ ;  $\lambda_r$ ,  $\lambda_w$ ,  $\lambda_g$ , and  $\lambda_h$  are the thermal conductivity coefficients of hydrate sediment rock–soil skeleton, water, methane gas, and methane hydrate,  $W/(m \cdot K)$ ;  $C_r$ ,  $C_w$ ,  $C_g$ , and  $C_h$  are the specific heat capacities of the hydrate sediment rock–soil skeleton, water, methane gas, and methane hydrate,  $kJ/kg \cdot K$ ;  $\Delta H$  is the decomposition enthalpy of methane hydrate,  $kJ/mol$ ; and  $\lambda_c$  is the equivalent thermal conductivity of hydrate reservoirs,  $W/(m \cdot K)$ .

## 2.3. Initial and Boundary Conditions

### 2.3.1. Initial Conditions

The initial conditions of saturation and salinity of each phase in the model are determined according to the methane hydrate reservoir in the South China Sea:

$$S_h = S_{h0}, S_g = S_{g0}, S_w = S_{w0}, X_s = X_{s0} \quad (r \leq R) \quad (12)$$

The initial temperature and pressure conditions of hydrate reservoirs in the model are determined according to the geothermal gradient and pressure gradient of the reservoir:

$$T = T_0 + \Delta z t_g \quad (13)$$

$$P = P_0 + \Delta z p_g \quad (14)$$

where  $T_0$  is the initial temperature of the uppermost layer of the hydrate reservoir,  $K$ ;  $t_g$  denotes the geothermal gradient of the stratum,  $K/m$ ;  $P_0$  is the initial pressure of the uppermost layer of the hydrate reservoir,  $MPa$ ; and  $p_g$  is the pressure gradient of the stratum,  $MPa/m$ .

### 2.3.2. Boundary Conditions

This study adopts a two-dimensional model, and the main boundary conditions include three parts.

The boundary on the lateral borehole sidewall of hydrate reservoirs is called boundary A. The vertical upper and lower boundary of hydrate reservoirs is called boundary B. The lateral outer boundary of hydrate reservoirs is called boundary C.

For boundary A, the drilling fluid in the wellbore is considered as the first boundary condition:

$$T = T_f, P = P_f, X_s = X_{sf}, S_h = 0, S_g = 0, X_s = X_{in} \quad (r = r_w) \quad (15)$$

For boundary B, the upper and lower boundary layers in the vertical direction are set to be the Dirichlet boundary condition in temperature and impermeable layers in pressure:

$$T = T_0 (z = 0), T = T_H (z = H) \quad (16)$$

For boundary C, the temperature at the far end of the hydrate reservoir is regarded as the Dirichlet boundary condition; therefore, the temperature of the outer boundary remains constant. As for the pressure, there are two main methods. The first is that the outer lateral boundary of the reservoir is regarded as an impermeable boundary, where there is no mass exchange and flow between the hydrate reservoir and the outer boundary, and the pressure is not affected by the outside of the calculation area. Second, the pressure of boundary C is set equal to the initial pressure and the temperature of boundary C is set equal to the initial temperature.

In this study, considering that the invasion range of drilling fluid is smaller than that of the calculation area, the outer boundary of the calculation area can be approximately regarded as unaffected by the outside environment, and therefore the second infinite extension boundary is selected.

$$T = T_0, P = P_0 (r = r_{base}) \quad (17)$$

#### 2.4. Numerical Solution of the Model

Based on the interaction between the mass transfer and heat transfer processes, the gas–liquid two-phase flow process, and the hydrate formation and decomposition processes, the above numerical model was established. In order to solve the model, the finite difference method was applied for the calculations in our simulation, and we wrote a program to solve all the discretized equations. The discretization processes of the specific model equations are shown in Equations (A1)–(A9) in Appendix A.

##### 2.4.1. Geological Setting of the Gas Hydrate Reservoir

The simulation target area of this study is the hydrate enrichment area at station W17 in the Shenhu sea area, which is a part of the Baiyun Sag of Pearl River Mouth Basin, as shown in Figure 1. The seabed topography of the target area is undulating, and the terrain is complex and changeable. As a whole, it descends vertically in steps, and the level is high in the north and low in the south. It has tectonic and geomorphological features such as troughs, sea valleys, seamounts, sea hills, steep slopes, steep ridges, submarine plateaus, submarine slumps that are more conducive to the formation of hydrates, and submarine fans. The hydrate reservoir is a tight argillaceous silt type. According to the preliminary analysis results of natural gas hydrate samples, the average seafloor heat flow value is about 76.0 mW/m<sup>2</sup>, and the pore water salinity mass fraction is between 2.90% and 3.15%. The seafloor sediments are mainly silt (32–63 μm), in which clay content is not less than 20%.

In 2017, China successfully implemented a short-term trial exploitation of the hydrate reservoir at this station. As shown in Figure 2, the deposit at station W17 is relatively thick, showing a north–south belt; the reservoir area is 6.42 km<sup>2</sup>, the maximum thickness can reach 95 m, the average available channel thickness is 57 m, and the reservoir has the characteristics of thick middle and thin edges. The hydrate reservoir at station W17 is located at a seawater depth of 1266 m and can be subdivided into two hydrate layers, with hydrate layer I being at 201–236 m below the seabed and hydrate layer II being at 236–251 m below the seabed [25].

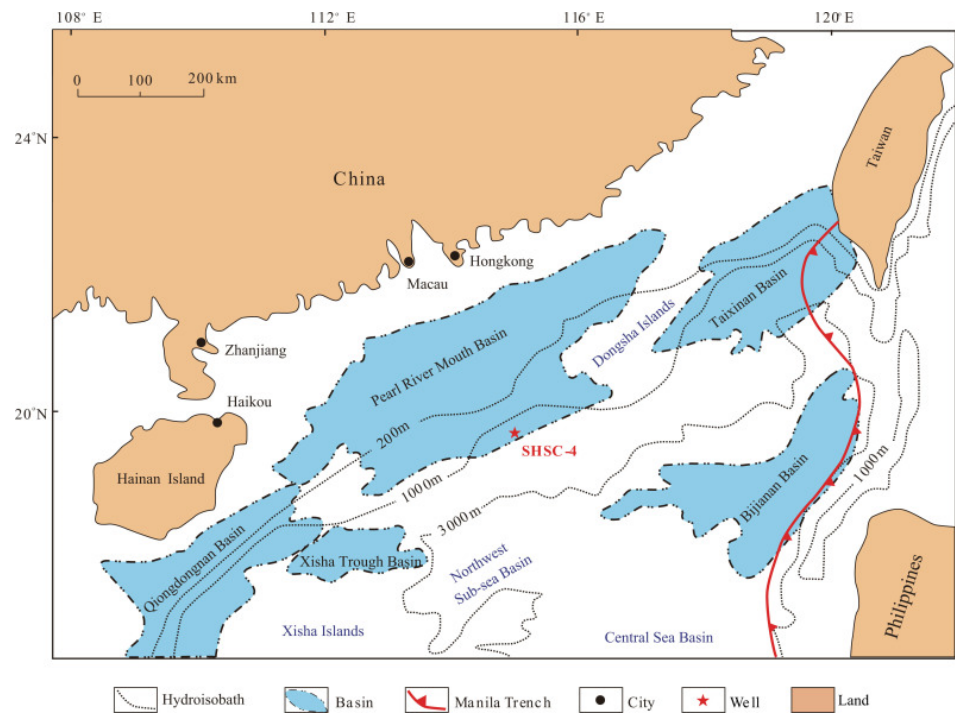


**Figure 1.** Trial production location of natural gas hydrate from the reservoir in the Shenhu sea area, South China Sea [25].

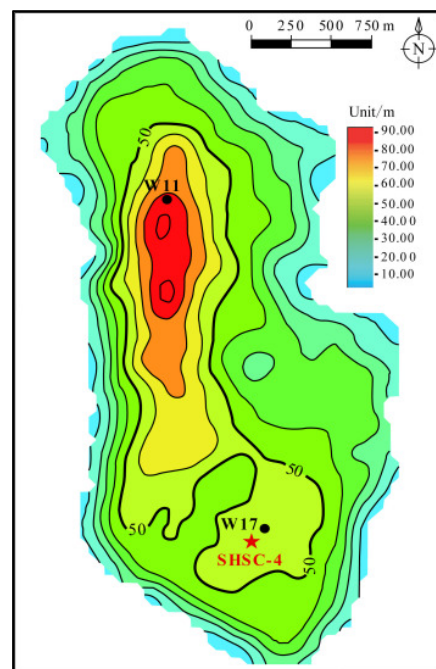


**Figure 2.** Schematic diagram of hydrate layer thickness distribution at W11 and W17 stations [25].

#### 2.4.2. Basic Parameters

Specific geological parameters include the inherent permeability of the formation, original reservoir pressure, bottom hole flowing pressure, and water–rock compressibility coefficient. The physical properties of the drilling fluid and hydrate reservoir are listed in Table 1.

**Table 1.** Parameters of the methane hydrate reservoir at station W17, South China Sea.

Parameter	Value	Parameter	Value
Initial layer I hydrate saturation/ $S_{ho1}$	0.34	Geotechnical specific heat capacity of frame/ $C_r$	0.71 kJ/kg·K
Initial layer II hydrate saturation/ $S_{ho2}$	0.31	Hydrate specific heat capacity/ $C_h$	2.1 kJ/kg·K
Initial layer I water saturation/ $S_{wo1}$	0.66	Methane specific heat capacity/ $C_g$	2.2 kJ/kg·K
Initial layer II water saturation/ $S_{wo2}$	0.612	Intrinsic permeability of layer I/ $k_{D0}$	$1.5 \times 10^{-15} \text{ m}^2$
Initial pore gas saturation of layer I/ $S_{go1}$	0	Intrinsic permeability of layer II/ $k_{D0}$	$2.9 \times 10^{-15} \text{ m}^2$
Initial pore gas saturation of layer II/ $S_{go2}$	0.078	Thermal conductivity of methane gas/ $\lambda_g$	0.07 W/(m·K)
Initial seawater mass density/ $\rho_w$	1019 kg/m <sup>3</sup>	Thermal conductivity of hydrate/ $\lambda_h$	0.6 W/(m·K)
Rock mass density of frame/ $\rho_r$	2600 kg/m <sup>3</sup>	Geotechnical thermal conductivity of frame/ $\lambda_r$	2.5 W/(m·K)
Mass density of hydrate/ $\rho_h$	920 kg/m <sup>3</sup>	Salt diffusion coefficient/ $K_{DD}$	$1.76 \times 10^{-9} \text{ m}^2/\text{s}$
Initial temperature of hydrate reservoir/ $T_0$	14.82 °C	Bottom hole flowing pressure/ $P_f$	15.6 MPa
Wellbore radius/ $r_{base}$	0.1 m	Enthalpy of hydrate decomposition/ $\Delta H$	54.2 kJ/mol

### 2.4.3. Mesh Generation

In this study, the numerical model of the process of drilling into the hydrate reservoir in a two-dimensional cylindrical coordinate system is developed. The inner boundary of the model is set as the wellbore with a radius of 0.1 m. The mesh is divided into lateral and axial directions.

The lateral direction mesh is divided into 80 elements, in which the element spacing is calculated according to the following formula:

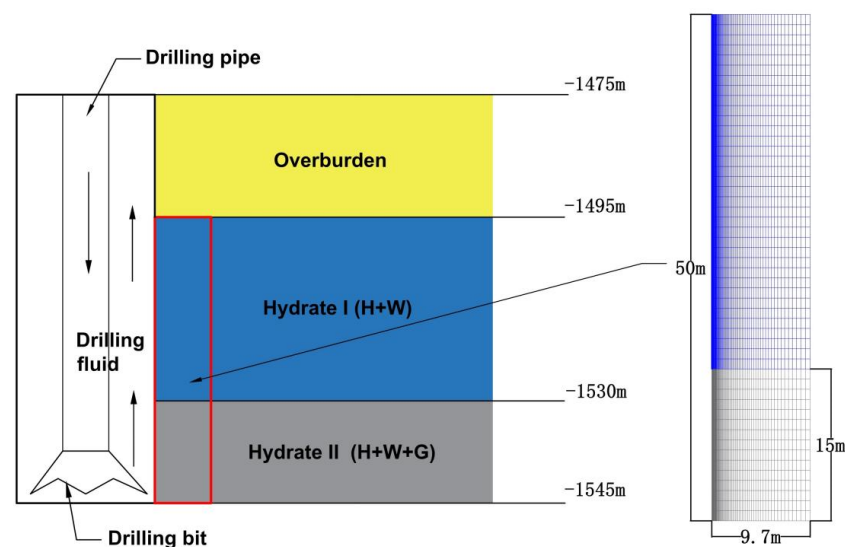
$$\Delta r = 0.01 \times 1.05^N \quad (18)$$

According to Figure A1, the closer the lateral grid spacing parameter is to 0.01 m, the closer the pressure distribution of the numerical simulation results is.

Regarding the axial direction, according to Figure A2, the simulation results for different vertical element spacings are basically the same. Therefore, the axial direction mesh is divided into 50 elements on average, and the height of each layer is 1 m; layers 1–15 are hydrate layer I, and layers 16–50 are hydrate layer II.

$$\Delta z = 1 \text{ m} \quad (19)$$

The mesh generation of the hydrate reservoir is shown in Figure 3.

**Figure 3.** Grid structure diagram.

#### 2.4.4. Solution Process

In order to clearly illustrate the numerical solution process of the mathematical model, a flow chart of the calculation process is shown in Figure 4.

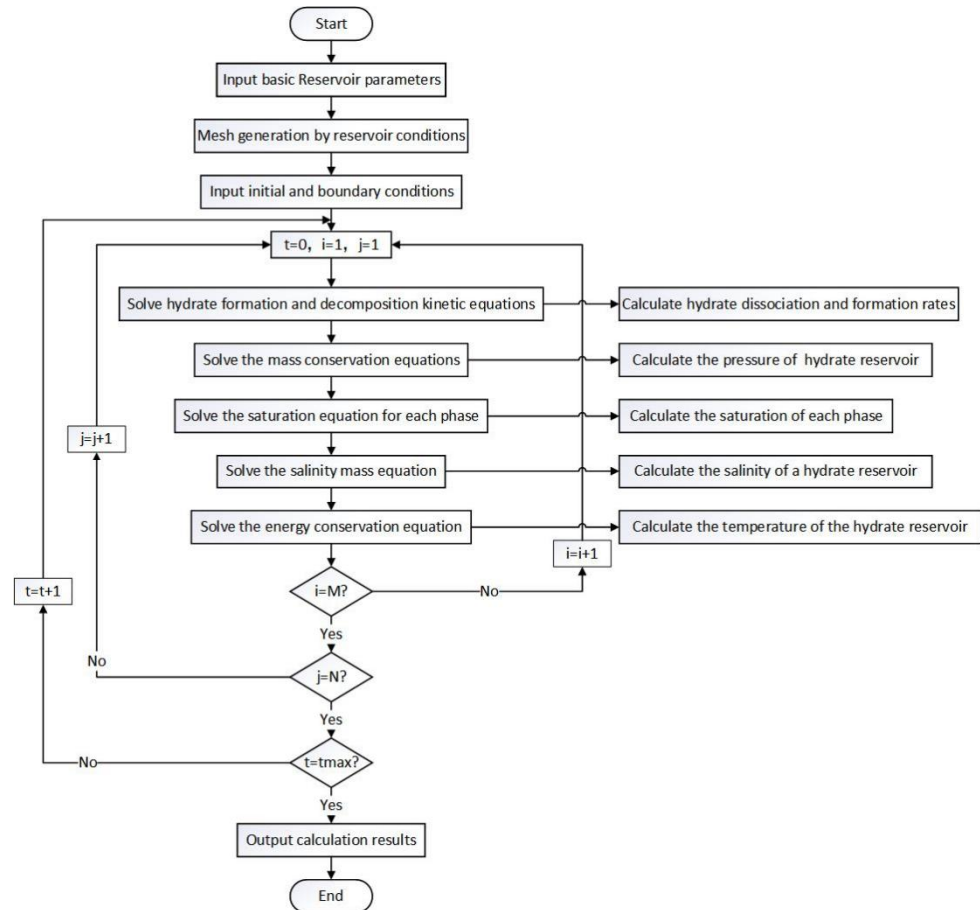


**Figure 4.** Flow chart of the process of the numerical solution.

The main numerical solution process is shown in Figure 4. In the calculation of a certain time, firstly, according to the input basic reservoir parameters, divided grid parameters, and the initial and boundary conditions, the dynamic equations of natural gas hydrate are solved, and the decomposition or formation rate of hydrate is calculated. Then, the pressure distribution of the reservoir is solved using the LU decomposition method combining the discrete equations, saturation equation, and capillary pressure equation. Subsequently, the mass conservation equation of each phase is solved to obtain the saturation of each phase and the salinity distribution of the reservoir. Finally, the energy conservation equation of the reservoir is solved using the LU decomposition method to obtain the temperature distribution of the reservoir at the next moment.

### 3. Results and Discussion

Based on the properties of the actual hydrate reservoir at the W17 station in the Shenhu sea area, a physical model was constructed, and the numerical model was solved using the method of self-programming. The numerical simulation study of the two-dimensional physical property response characteristics of drilling fluid intrusion into hydrate reservoirs during the drilling of natural gas hydrate in offshore areas was carried out; the effects of drilling fluid temperature and salinity on the decomposition and secondary hydrate formation characteristics of hydrate during the invasion process were studied.

### 3.1. Response of Reservoir Physical Properties during Drilling Fluid Invasion

Figure 5 shows the simulated distribution of the pressure, temperature, salinity, and saturation of each phase in the hydrate reservoir around the wellbore at the 24th hour of the drilling process with the drilling fluid temperature of 16 °C and salinity of 3.05 wt%. Figure 5a displays the pressure distribution of the reservoir. It can be seen that under the function of pressure differential, the drilling fluid displaces the original fluid in the pores around the wellbore into the hydrate reservoir, leading to an increase in the reservoir pore pressure. In the vertical direction, in the area close to the wellbore, the pressure in layer II is higher than that in layer I, while the pressure in the area far from the wellbore in layer II is a little lower than that in layer I. It can be found from the hydrate saturation distribution in Figure 5c that a small amount of hydrate is formed in layer II in a wide range. This is due to the difference in reservoir physical properties at different heights of strata. There is only water and hydrate in layer I, but there is a small amount of methane gas in layer II. During the invasion of drilling fluid, a small amount of hydrate is formed in layer II, which will consume some water and methane gas and release heat, leading to a decrease in pressure and increase in temperature in layer II.

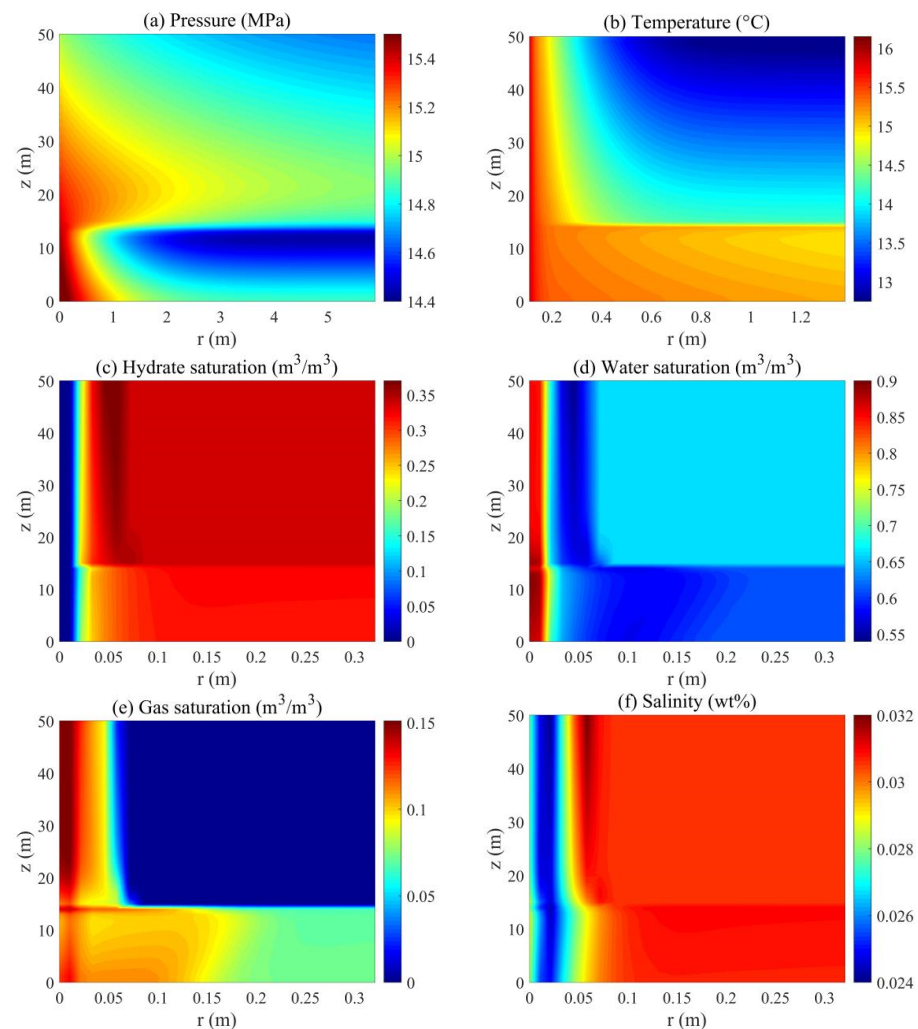


**Figure 5.** Two-dimensional physical distribution of the hydrate reservoir at the 24th hour of the invasion process of drilling fluid. (a) Pressure distribution; (b) temperature distribution; (c) hydrate saturation distribution; (d) water saturation distribution; (e) gas saturation distribution; (f) salinity distribution.

As shown in Figure 5a, the pressure decrease area in layer II is larger than that in layer I with the increase in the distance from the wellbore. This may be because layer II contains a small amount of free gas, resulting in secondary hydrate formation. However, gas has higher compressibility, resulting in faster attenuation during pressure propagation.

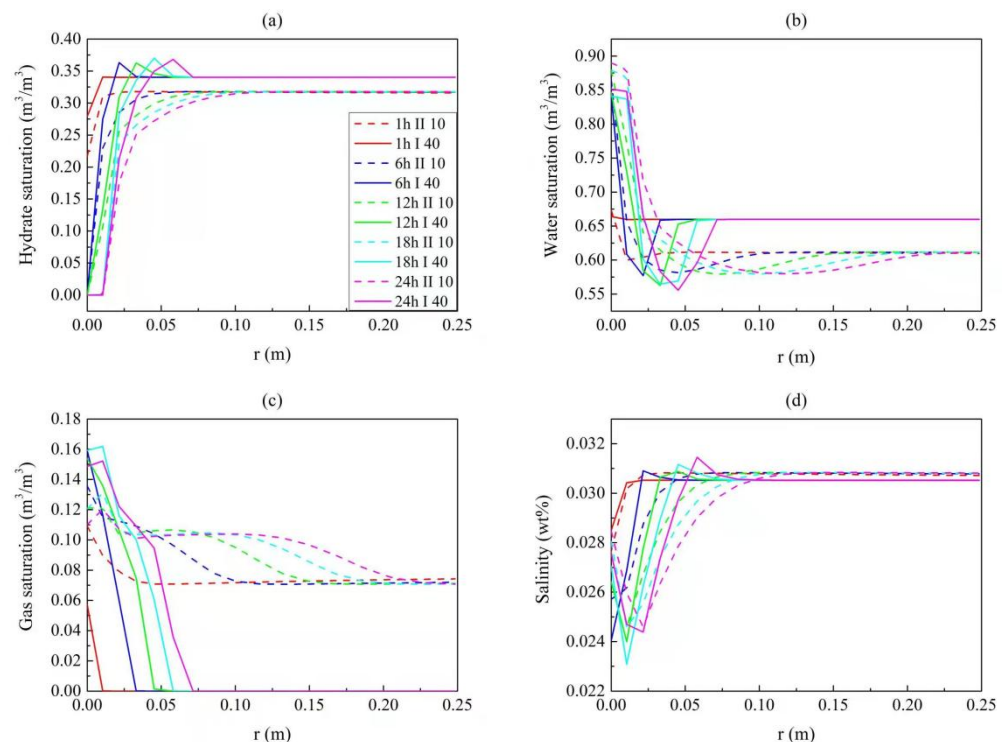
Figure 5b shows the temperature distribution in the reservoir. In radial distribution, the overall tendency of temperature distribution in the radial stratum is similar to that of pressure distribution. The rate of temperature change in layer II is greater than that in layer I. On the basis of the geothermal gradient of the reservoir, the temperature of layer II is obviously higher than that of layer I, and there is a large-scale increase in the radial direction.

Figure 5c–e exhibit the simulated distributions of gas, water, and hydrate saturations in the reservoir. Due to the increase in temperature in the reservoir, a dark blue area near the wellbore, where the hydrate has been completely decomposed, can be seen in Figure 5c. Correspondingly, the water and gas saturations increase as a result of a large amount of water and methane gas produced by the hydrate decomposition in the reservoir. The water saturation in layer II near the wellbore is higher than that in layer I, which may be due to the higher invasion rate of drilling fluid in layer II, and subsequently, drilling fluid entering the reservoir increases the water saturation. As shown in Figure 5c, during the drilling process, the decomposition of hydrate occurs in a region near the wellbore, not a decomposition surface, which divides the hydrate reservoir into a decomposed area and a non-decomposed area, as a result of the salinity distribution [23]. There is a high hydrate saturation zone in layer I near the area where hydrates are decomposed. It is due to the fact that a large amount of water and methane gas is generated from the hydrate decomposition in the reservoir, and the methane gas forms hydrate again under certain temperature and pressure conditions [30], which is called “secondary hydrate formation”. Additionally, a large amount of water will be consumed in the process of secondary hydrate formation. Correspondingly, a zone with low water saturation can be found at the same position in Figure 5d. However, in the area near the wellbore in layer II, there is not an area with a large amount of secondary hydrate formed. This is due to the faster pressure attenuation and higher temperature in layer II, resulting in no temperature and pressure conditions suitable for a large amount of secondary hydrate formation. In this study, the methane gas is set to be 100% methane gas. The gas composition in different hydrate reservoirs is various, resulting in a difference in the equilibria and kinetics of the hydrate, which affect the hydrate decomposition and reformation, as well as the phase distribution in the reservoir. Figure 5f illustrates the simulated distribution of the pore water salinity in the reservoir. The water produced by the decomposition of hydrate will decrease the salinity of the pore water in the reservoir, and a zone with low salinity occurs in the domain around the wellbore. However, the salinity of the reservoir around the wellbore will increase to a certain extent again due to the invasion of drilling fluid. The secondary hydrate occurs in the high salinity zone, and the salinity of pore water increases obviously and is higher than that of pore water in the original reservoir.

Overall, the temperature and pressure of the hydrate reservoir around the wellbore will rise to varying degrees during the drilling process. The stable existence of natural gas hydrate requires specific temperature and pressure conditions, and the changes in pressure and temperature will inevitably lead to hydrate decomposition for reformation, changing the saturations and distributions of the water and methane gas in the reservoir and then affecting the salinity of the pore water. In general, in layer I, in which there is no free gas, the formation temperature is low, the drilling fluid invasion and hydrate decomposition speed are slow, the heat transfer has a greater impact on the reservoir, the hydrate decomposition area is small, the secondary hydrate formation is obvious, and the salinity increase area is small. In layer II, there is free gas and the temperature is high: the drilling fluid invasion and hydrate decomposition speed are faster, the influence of convective heat transfer on hydrate decomposition increases, the hydrate decomposition

area is large, the secondary hydrate formation is not obvious, and the salinity increase near the wellbore is more obvious.

The physical properties of the hydrate reservoir are significantly different in the vertical direction due to reservoir temperature and pressure gradients and the different types of reservoirs, resulting in different response characteristics in the reservoir during the drilling process. Figure 6 shows the distribution of physical properties of the hydrate reservoir at 10 m and 40 m from the reservoir bottom at different times during the drilling process.



**Figure 6.** Physical property distribution curves of layer II at 10 m from the bottom of the hydrate reservoir and layer I at 40 m from the bottom of the hydrate reservoir at different drilling fluid invasion times: (a) hydrate saturation distribution curves; (b) water saturation distribution curves; (c) gas saturation distribution curves; (d) salinity distribution curves.

The differences in the saturations of hydrate, gas, and water mainly come from the difference in initial saturation of strata and the difference in decomposition and secondary formation of hydrate in the vertical direction. Due to the temperature gradient of the hydrate reservoir, the temperature of layer I in the reservoir is lower and conducive to secondary hydrate formation. Therefore, it can be seen from Figure 6a that there is an area in layer I with higher hydrate saturation than the initial hydrate saturation. The area of the secondary hydrate formation zone expands and moves away from the wellbore. However, layer II of the reservoir contains only a small amount of secondary hydrate. The secondary hydrate formation consumes a large amount of water, as shown in Figure 6b, in which a depression area with low water saturation corresponds to the secondary hydrate formation area. The water saturation decreases more sharply with time, and the range of decrease is also larger. In layer II, the change in water saturation is mainly affected by the hydrate decomposition, and there is a wider range with a gentler pressure reduction.

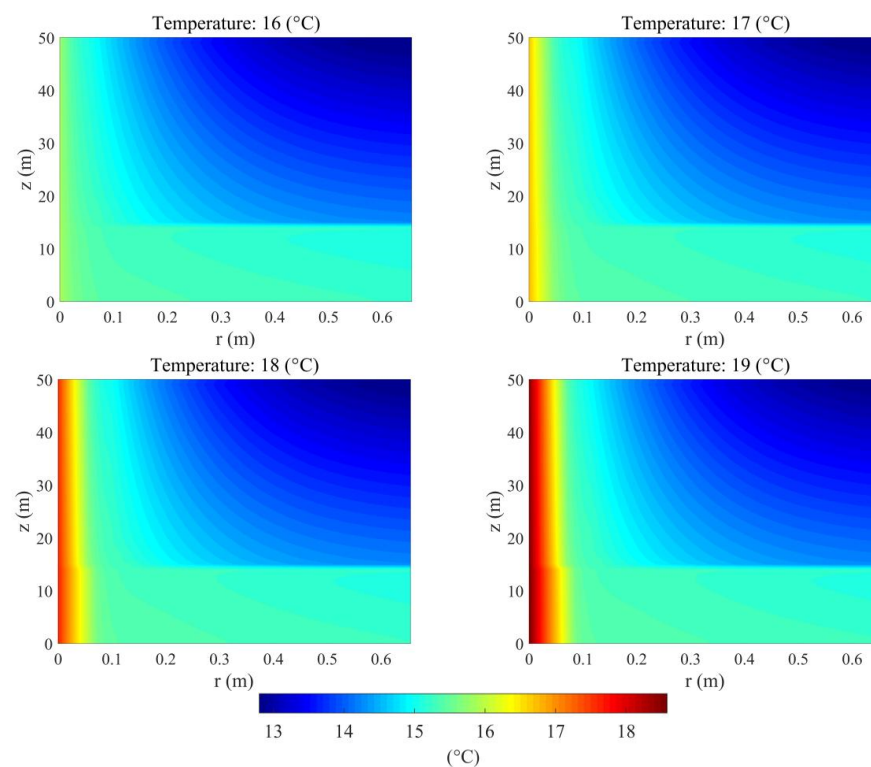
As shown in Figure 6b,c, in layer I, the change ranges of the gas and water saturations are mainly within the area of secondary hydrate formation, indicating that the secondary formation of hydrate prevents gas and water from spreading further to farther regions. However, in layer II, the change ranges of the gas and water saturations are much larger than the change range of the hydrate saturation, indicating that the diffusion of gas and water is much easier because there is not an area with high saturation of secondary hydrate

and free gas in layer II. At different times, the radial variation behaviors of saturations of different phases are similar, and over time, this observation progresses to the region far from the wellbore.

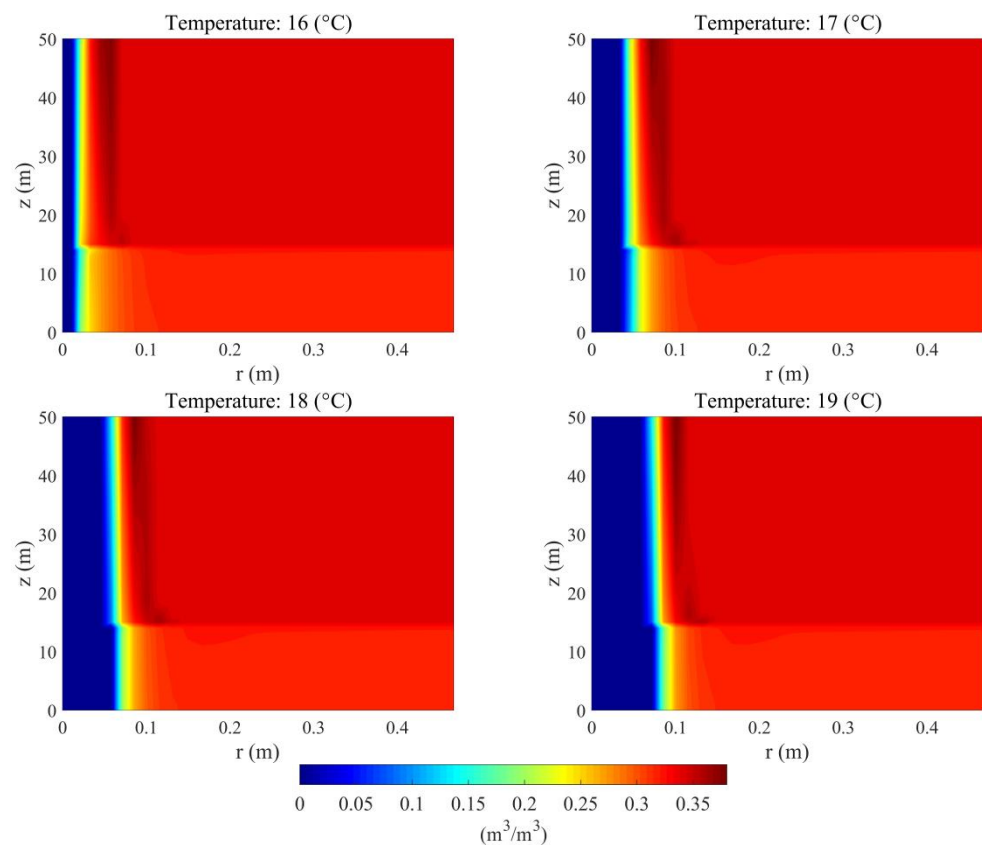
### 3.2. The Influence of the Drilling Fluid Temperature

Compared with the drilling process in conventional oil and gas reservoirs, the drilling process in hydrate reservoirs should take hydrate stability into account. Previous research shows that an increase in drilling fluid temperature will promote hydrate decomposition under the same pressure and drilling fluid salinity. In this study, the influence of the drilling fluid temperature on the properties of the reservoir near the wellbore was simulated.

Figure 7 shows the simulated temperature distribution of the hydrate reservoir under various drilling fluid temperatures of 16 °C, 17 °C, 18 °C, and 19 °C with the salinity of 3.05 wt%. The heat transfer from the drilling fluid to the reservoir as a result of the convection and conduction raises the hydrate reservoir temperature. The higher the temperature of the drilling fluid, the greater its influence on the reservoir. For various drilling fluid temperatures, the difference in the reservoir temperature is mainly concentrated in the near-wellbore area, and the temperature perturbation farther away from the wellbore area is not very obvious. This is explained by the observation that the heat transferred from the wellbore is mainly consumed by hydrate decomposition. Figure 8 describes the distribution of the hydrate saturation in the reservoir under various drilling fluid temperatures. The difference in the drilling fluid temperature is reflected in the different amounts of hydrate decomposition in the area near the wellbore. In this study, when the drilling fluid temperature increases from 16 °C to 19 °C, the range of hydrate decomposition has a significant increase. This indicates that the control of the drilling fluid temperature is of great importance to the hydrate decomposition in the reservoir and the wellbore stability. Under the high temperature of the drilling fluid, secondary hydrate formation can still be observed in layer I.



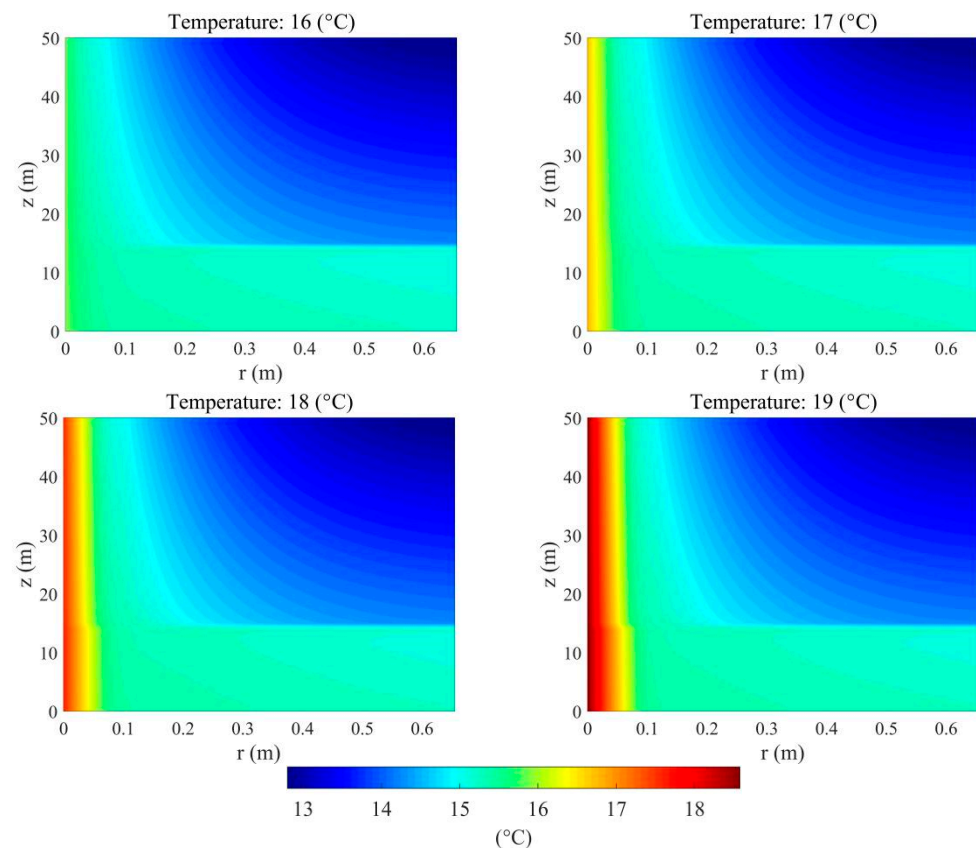
**Figure 7.** Comparison of two-dimensional temperature distribution of hydrate reservoirs for a fixed salinity of 3.05 wt% at the 24th hour of drilling fluid invasion under different drilling fluid temperatures.



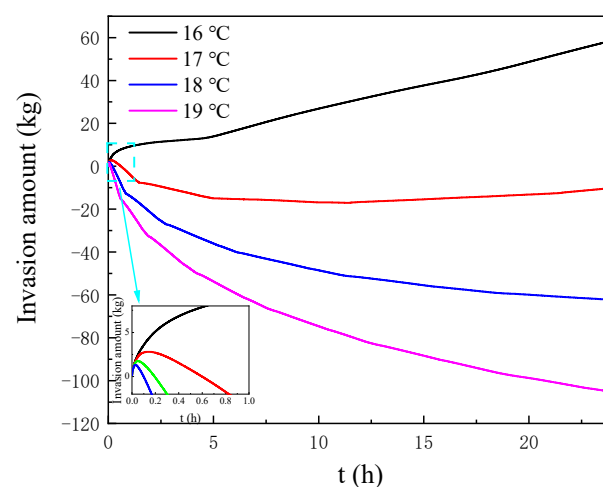
**Figure 8.** Comparison of two-dimensional hydrate saturation distribution of hydrate reservoirs for a fixed salinity of 3.05 wt% at the 24th hour of drilling fluid invasion under different drilling fluid temperatures.

Figure 9 shows the simulated water saturation distribution of the reservoir under various drilling fluid temperatures. There is a high water saturation zone in the hydrate decomposition area and a low water saturation zone in the secondary hydrate formation area. The range of the high water saturation zone increases with the increase in drilling fluid temperature, similar to the hydrate decomposition range under various drilling fluid temperatures. However, in the area of hydrate decomposition, the water saturation under the high drilling fluid temperature is significantly lower than that under the low drilling fluid temperature. In this study, the drilling fluid pressure is higher than that in the original reservoir. Therefore, the water from the decomposed hydrate will flow into the region far from the wellbore, resulting in a decrease in the water saturation. Another possibility is that the hydrate dissociation under the high drilling fluid temperature is fast, resulting in the high local pressure in the hydrate decomposition area. This pressure may be higher than that of the drilling fluid, causing the water and gas decomposed from the hydrate to flow into the wellbore. We calculated the changes in the amount of the drilling fluid invading the reservoir under various drilling fluid temperatures at the 24th hour, as shown in Figure 10. From the beginning of the drilling, the invasion amount of the drilling fluid increases continuously with time under the drilling fluid temperature of 16 °C. In other cases, the invasion of the drilling fluid only lasts less than 10 min. Subsequently, the invasion amount of the drilling fluid decreases continuously. Particularly, under the drilling fluid temperatures of 18 °C and 19 °C, the invasion amount of the drilling fluid keeps decreasing during the whole drilling process. The decrease in the invasion amount of the drilling fluid actually indicates that the fluid in the reservoir flows into the wellbore. This may be because the pressure in the reservoir increases quickly and increases to the extent of being higher than that of the drilling fluid. The gas dissociated from hydrate also would flow with the water into the wellbore, causing the performance of the drilling fluid

to decrease. It can be found that the increase in drilling fluid temperature may significantly increase the possibility of gas invasion during the drilling in the hydrate reservoir. As shown in Figure 7, the temperature increase in the reservoir around the wellbore is high at a higher drilling fluid temperature. This indicates that the heat transfer from the drilling fluid to the reservoir is mainly caused by heat conduction at the drilling fluid temperatures of 17, 18, and 19 °C because there is no invasion of the drilling fluid and no heat transfer caused by heat convection.



**Figure 9.** Comparison of two-dimensional water saturation distribution of hydrate reservoirs for a fixed salinity of 3.05 wt% at the 24th hour of drilling fluid invasion under different drilling fluid temperatures.



**Figure 10.** Variation in drilling fluid invasion amount with time within 24 h during the drilling fluid invasion process under different drilling fluid temperatures.

As shown in Figure 10, for the drilling fluid temperature of 17 °C, as the drilling process progresses, the invasion amount starts to rise again, which may be caused by the pressure of the reservoir dropping below the drilling fluid pressure. For the drilling fluid temperatures of 18 °C and 19 °C, the downward trends also tend to be gentle. This indicates that the phenomenon of gas invasion into the wellbore occurs mainly in the early stage of the drilling process. During this period, it is crucially important to control the drilling fluid temperature to prevent the hydrate decomposition in the reservoir.

The pressure behavior in the reservoir during the drilling process is the determining factor of the fluid flow. Figure 11 displays the evolutions of the simulated pressure distribution in the reservoir with the drilling fluid temperature of 19 °C at 10 m and 40 m from the bottom of the reservoir. As shown in Figure 11, the pressure in layer I of the reservoir increases first and then decreases quickly with the increase in distance from the wellbore. There is still an area with pressure higher than the drilling fluid pressure at the 24th hour. It conforms to Figure 10; the invasion amount of drilling fluid falls below 0 and then decreases continuously at the high drilling fluid temperature. In layer II, at the 24th hour, the pressure around the wellbore begins to flatten and the drilling fluid can continue to invade the hydrate reservoir. The simulation results indicate that in the reservoir with the low permeability and low gas saturation, the pressure increase caused by hydrate decomposition cannot be transmitted to the area far from the wellbore, resulting in the pressure rise around the wellbore and the flow of fluid in the reservoir into the wellbore. Therefore, it is of great significance to optimize the drilling operation and control the hydrate decomposition during drilling in hydrate reservoirs with similar conditions, such as the eastern enrichment area of the hydrate layer in the Nankai Trough of Japan [31] and the natural gas hydrate reservoir on the continental margin of India [32].

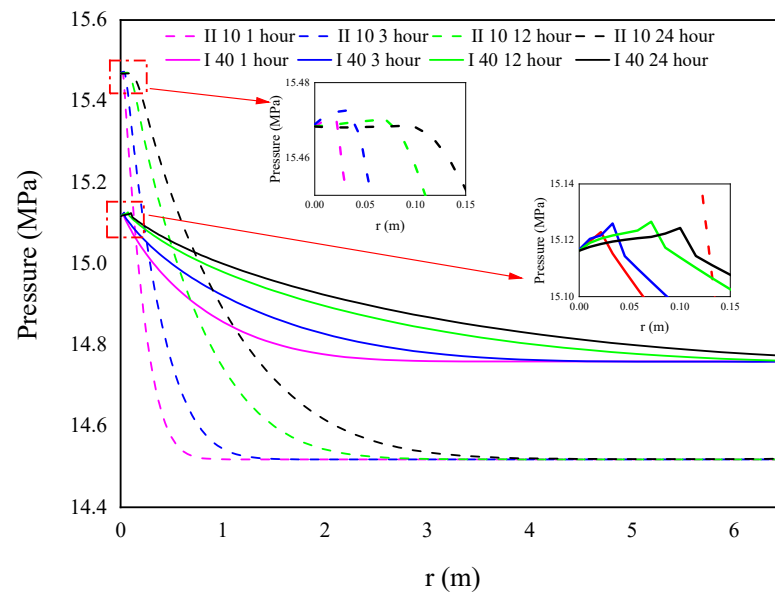


**Figure 11.** Pressure distribution curves of layer II at 10 m from the bottom of the reservoir and layer I at 40 m from the bottom of the reservoir under different drilling fluid invasion time conditions when the drilling temperature is 19 °C.

The phase transition of hydrate and drilling fluid invasion have a significant influence on the salinity of the pore water in the reservoir. Therefore, the drilling fluid temperature, which affects both the hydrate decomposition and drilling fluid invasion, also has a significant influence on the salinity distribution in the hydrate reservoir. Figure 12 shows the simulated salinity distribution in the hydrate reservoir near the wellbore under various drilling fluid temperatures. The main difference is that under the high drilling fluid temperature, there is a large area of hydrate dissociation and thus a large area of salinity drop. When the drilling fluid temperature is 16 °C, the salinity of the hydrate decomposition

area is significantly higher than that of the hydrate decomposition areas in other cases. This is due to the observation that when the drilling fluid temperature is 16 °C, there is no gas invasion and the drilling fluid invades into the reservoir during the whole drilling process, causing the salinity of the hydrate decomposition area to increase significantly. When the drilling fluid is at other temperature conditions, the salinity rise area near the wellbore decreases with the increase in the drilling fluid temperature at the 24th hour. This phenomenon is consistent with the variation in drilling fluid invasion amount under various drilling fluid temperatures, as shown in Figures 10 and 11.

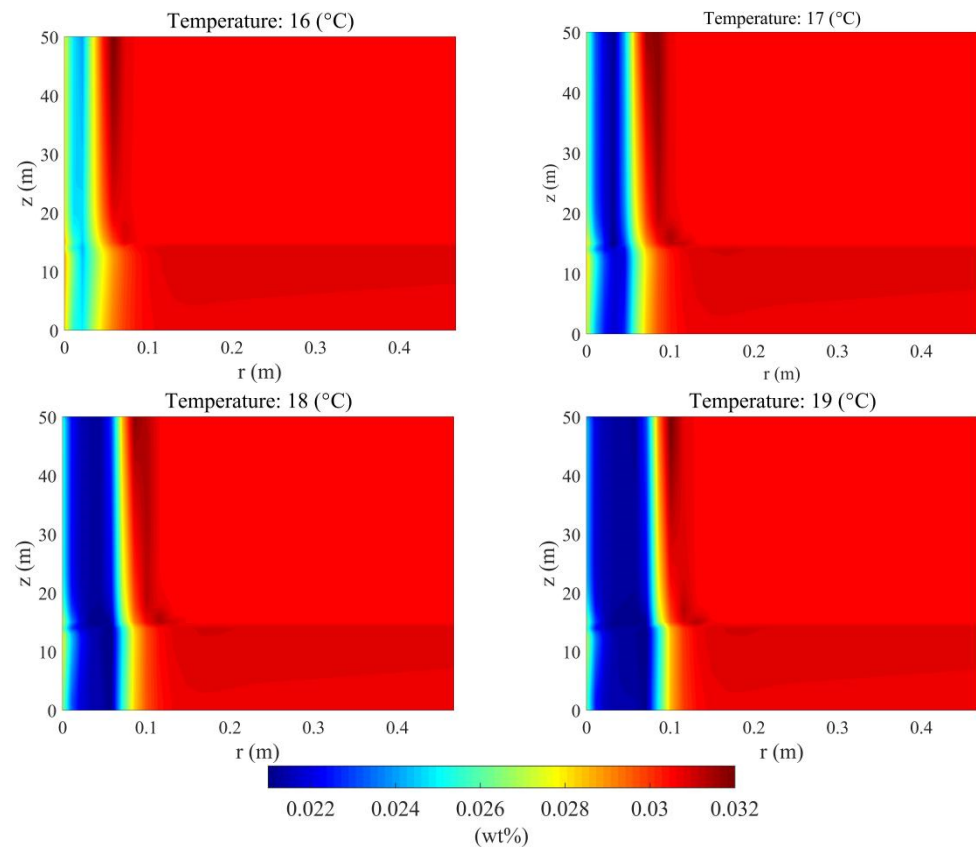


**Figure 12.** Comparison of two-dimensional salinity distribution of hydrate reservoirs for a fixed salinity of 3.05 wt% at the 24th hour of drilling fluid invasion under different drilling fluid temperatures.

### 3.3. The Influence of the Drilling Fluid Salinity

Figure 13 illustrates the simulated temperature distribution in the reservoir during the drilling process under various drilling fluid salinity values with the drilling fluid temperature of 16 °C. As shown in Figure 12, the drilling fluid salinity has little influence on the temperature perturbation range in the hydrate reservoir. This indicates that the drilling fluid salinity may have little influence on the heat transfer during the drilling process.

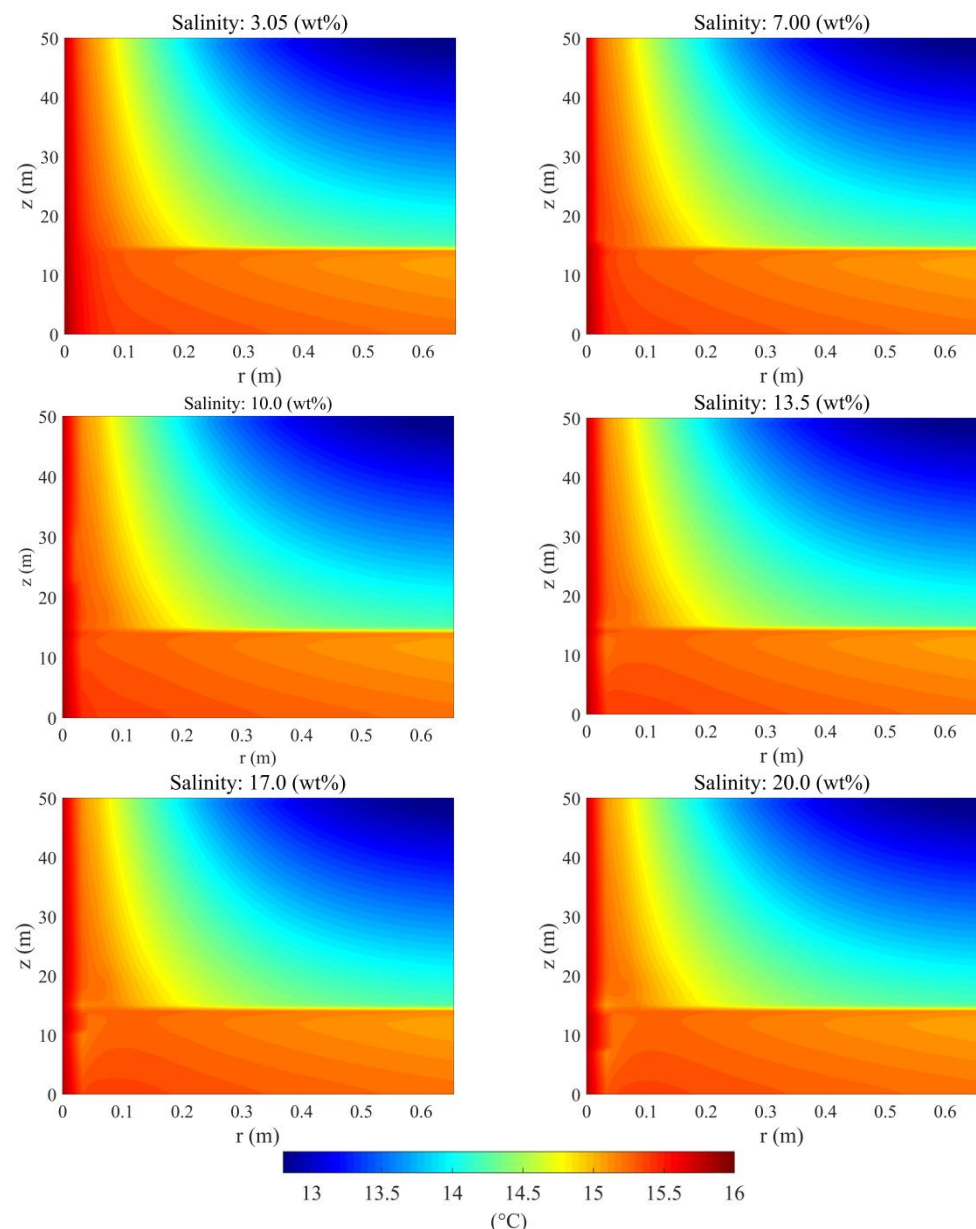


**Figure 13.** Comparison of two-dimensional temperature distribution of hydrate reservoirs for a fixed temperature of 16 °C at the 24th hour of drilling fluid invasion under various drilling fluid salinity values.

Figure 14 shows the hydrate saturation distribution of the reservoir under various drilling fluid salinity values. The distribution of the hydrate saturation can truly reflect the hydrate decomposition and formation in the reservoir during the drilling process. It can be found that the decomposition range of hydrate increases with the increase in the drilling fluid salinity since the increase in salinity will enhance the driving force for hydrate decomposition. The more hydrate decomposed generates more water and gas, the more secondary hydrate forms in layer I of the reservoir. It also can be found that the totally dissociated area of the hydrate under lower salinity is smaller than that under higher salinity. However, the range of the hydrate decomposed is much wider, especially in layer II under the salinity of 3.05 wt%, where the hydrate saturation gradually decreases in a wide range from the wellbore. It is speculated that the higher salinity could increase the hydrate decomposition rate but cannot bring more heat. Therefore, the high drilling fluid salinity causes the hydrate to decompose in a small area, and the temperature decrease

caused by the hydrate decomposition hinders the hydrate decomposition in the area far from the wellbore. In contrast, under low salinity conditions, the hydrate decomposition rate is low, and the hydrate could decompose in a large area around the wellbore.

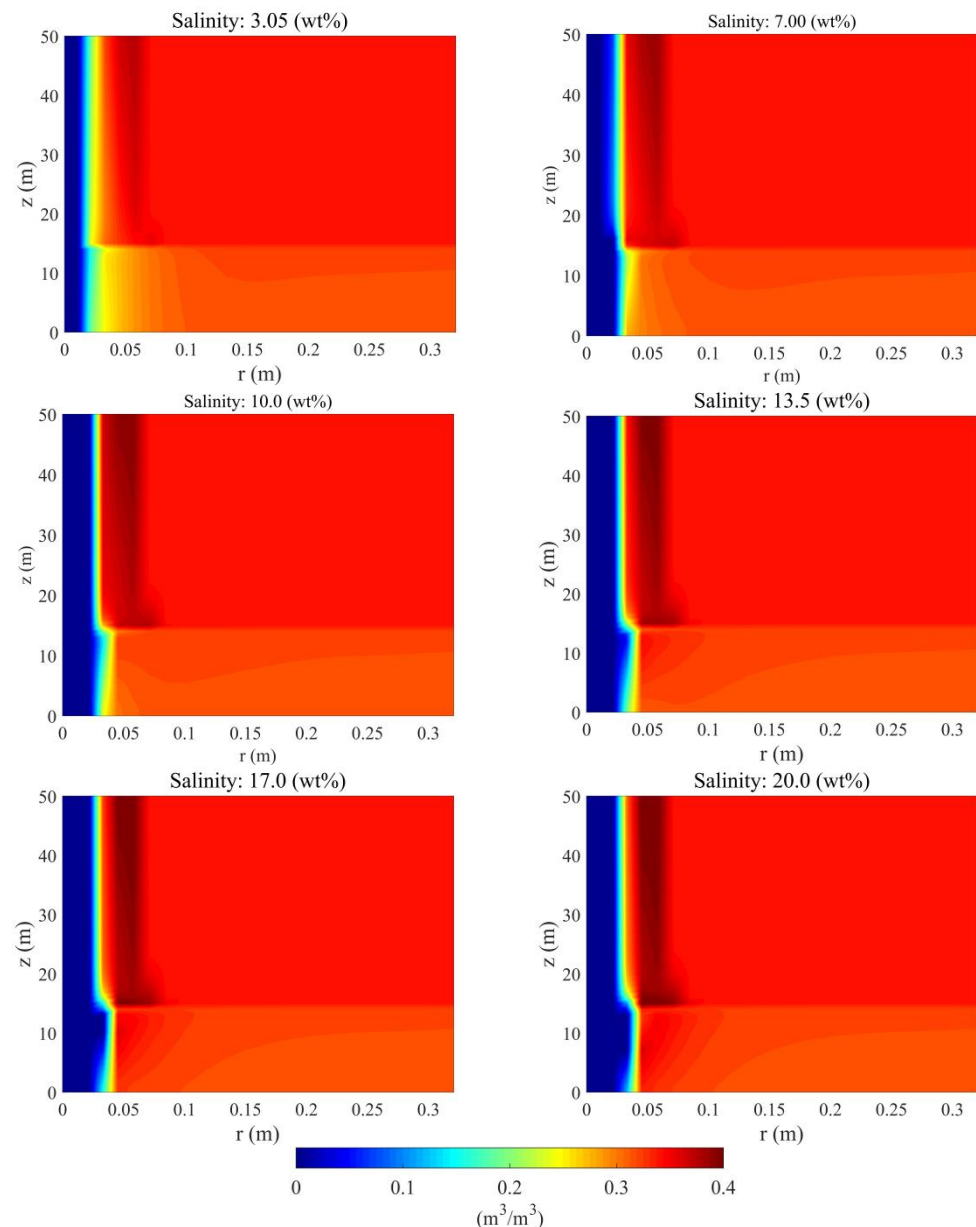
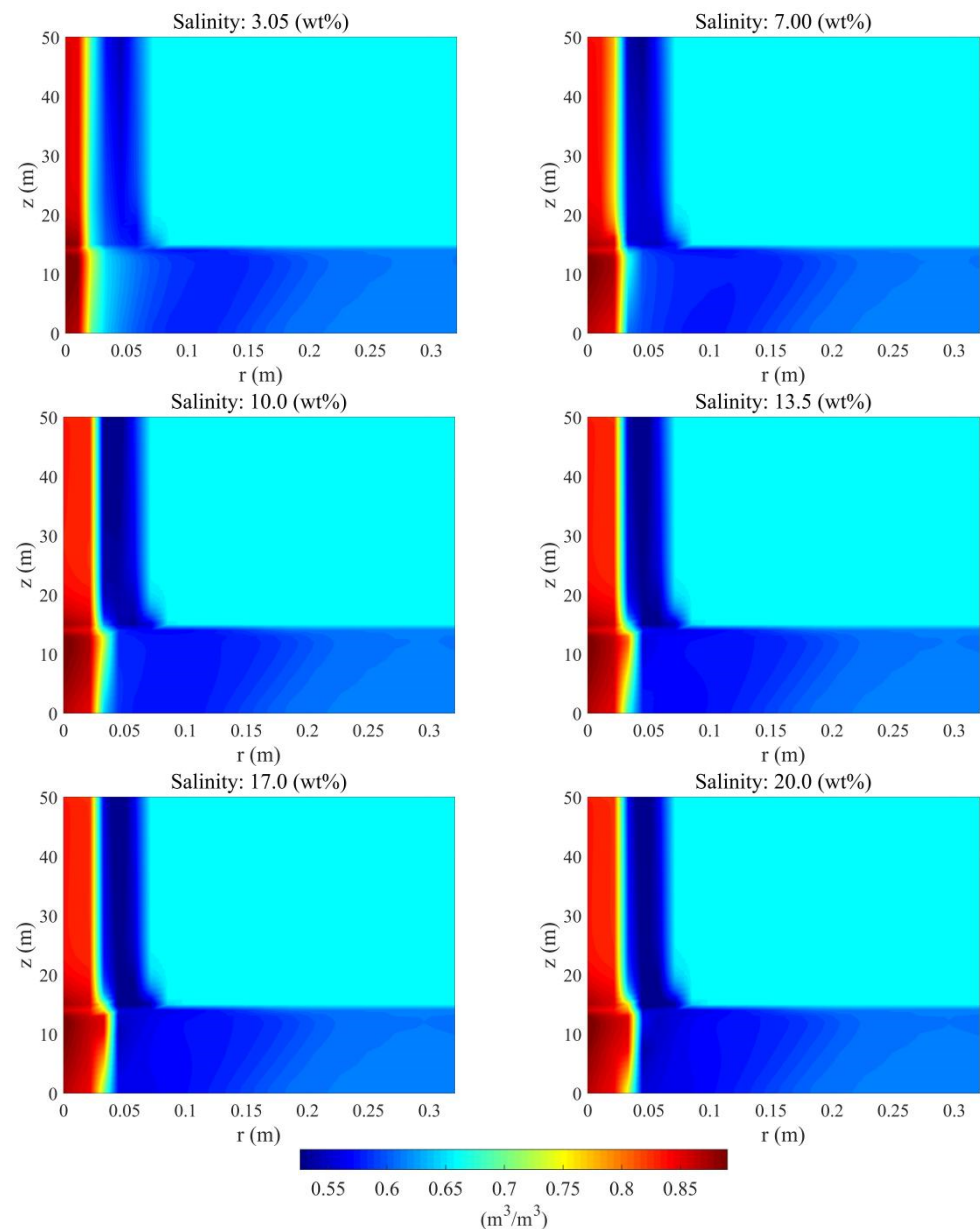


**Figure 14.** Comparison of two-dimensional hydrate saturation distribution of hydrate reservoirs for a fixed temperature of 16 °C at the 24th hour of drilling fluid invasion under various drilling fluid salinity values.

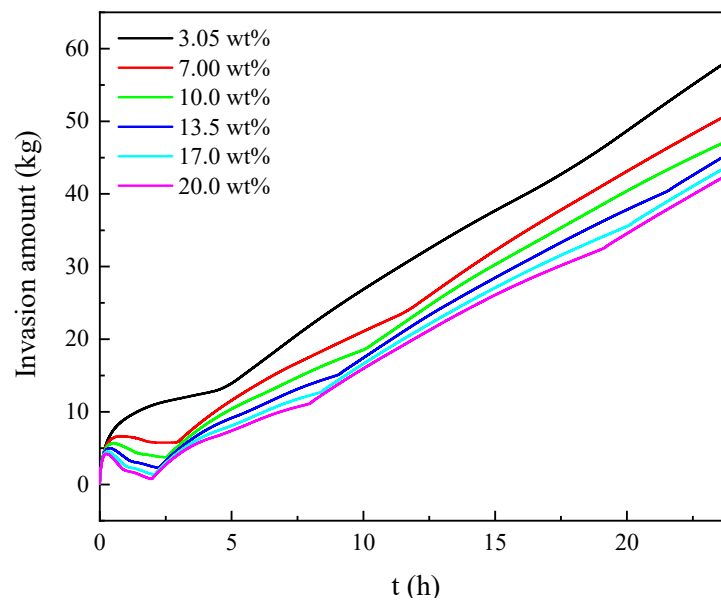
As shown in Figure 14, when the salinity exceeds 10 wt%, with the increase in drilling fluid salinity, the effect of the salinity on the decomposition of hydrate in the reservoir becomes weak. As discussed above, there is no clearly distinct difference in the heat brought from the drilling fluid with various salinity values compared to that with various drilling fluid temperatures. When the salinity reaches a certain level, the promotion effect of the salt on the hydrate decomposition becomes less pronounced due to the lack of enough heat for hydrate decomposition.

Figure 15 shows the simulated water saturation distribution in the reservoir under various drilling fluid salinity values. It is found that the area of low water saturation has hardly changed with the increase in drilling fluid salinity, which is consistent with

the increasing secondary hydrate formation in Figure 14. Related to the distribution of the hydrate saturation in Figure 14, the area where the water saturation increases under the low salinity is wide but the increase range is small. However, in contrast to Figure 9, the water saturation around the wellbore is high and shows no clear differences under various drilling fluid salinity values. A possible explanation of this observation may be that the drilling fluid salinity has a lesser impact than the temperature on promoting the decomposition of hydrate, and the pressure of the reservoir around the wellbore does not exceed the drilling fluid pressure, not leading to a large amount of fluid in the reservoir flowing into the wellbore. This can be also verified in Figure 16, which shows the evolution of the amount of the drilling fluid invading the hydrate reservoir.



**Figure 15.** Comparison of two-dimensional water saturation distribution of hydrate reservoirs for a fixed temperature of 16 °C at the 24th hour of drilling fluid invasion under various drilling fluid salinity values.



**Figure 16.** Variation in drilling fluid invasion amount with time within 24 h during the drilling fluid invasion process under various drilling fluid salinity values.

Overall, as shown in Figure 16, the invasion amount of the drilling fluid decreases with the increase in the drilling fluid salinity, and the difference occurs primarily in the first three hours. During the first three hours of the drilling process, the invasion amount of the drilling fluid first increases and then decreases with time under the drilling fluid salinity of 7–20 wt%. In the early stage of the drilling process, the hydrate decomposes quickly due to the high hydrate saturation of the reservoir, which results in a large amount of water and gas produced in a short time and causes the pore pressure around the wellbore to rise sharply. Finally, it will lead to the flow of pore fluid to the wellbore, further leading to the decrease in the invasion amount of the drilling fluid.

In the early stage of the drilling process, the hydrate saturation of the reservoir is high and the hydrate decomposes quickly, resulting in a large amount of water and gas produced in a short time. This may cause the pore pressure around the wellbore to rise sharply and lead to the flow of pore fluid to the wellbore and a decrease in the invasion amount of the drilling fluid. However, when the hydrate decomposes to a certain extent, the pressure of the reservoir around the wellbore drops to be lower than the drilling fluid pressure again, and the drilling fluid continues to invade the hydrate reservoir. In contrast to that, under high drilling fluid temperatures, the cumulative invasion amount of the drilling fluid always remains above null, and after 3 h, the increase rates under various drilling fluid salinity values show no obvious discrepancy. This also proves that the decomposition rate of the hydrate near the wellbore in the reservoir increases with the increase in the drilling salinity, causing a higher pressure increase and more fluid flowing back to the wellbore in the early stage. However, in the later stage, the promoting effect of the increasing salinity on the hydrate decomposition becomes weaker.

Figure 17 exhibits the salinity distribution of the reservoir under various drilling fluid salinity values. As shown in Figure 17, the salinity shows significantly different patterns under various drilling fluid salinity values. As shown in Figure 17, the salinity of the reservoir around the wellbore increases with the increase in drilling fluid salinity, even when the invasion amount of the drilling fluid is lower under the high drilling fluid salinity. This is due to the observation that when the drilling fluid salinity is higher than the pore water salinity in the reservoir, the invasion of the drilling fluid will considerably affect the salinity of pore water in the reservoir. The salinity of layer II increases faster than that of layer I, which is due to the free gas in layer II making the invasion of the drilling

fluid easier than that in layer I, in which the fluid has more difficulty flowing and the salt diffuses slower.

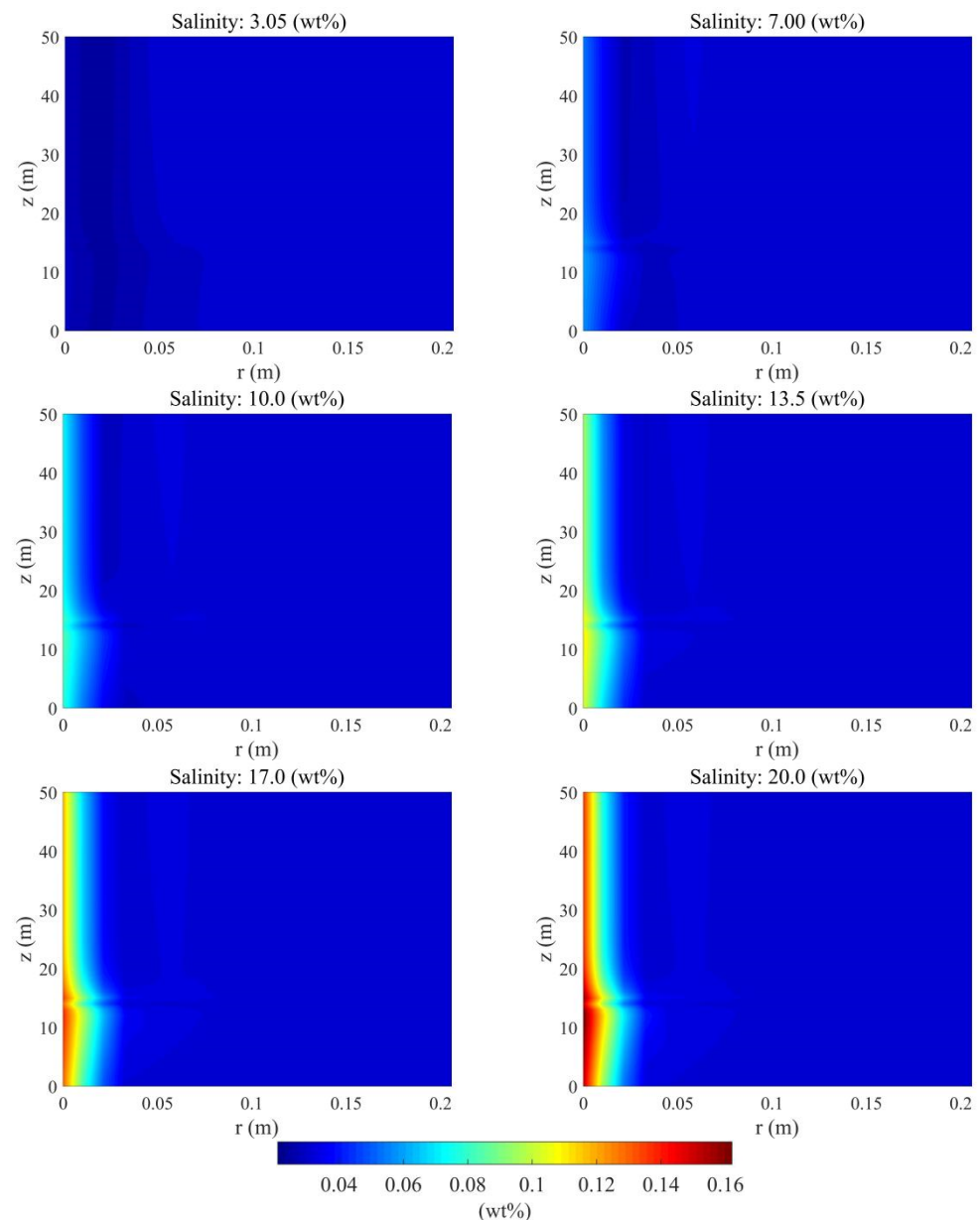


**Figure 17.** Comparison of two-dimensional salinity distribution of hydrate reservoirs for a fixed temperature of 16 °C at the 24th hour of drilling fluid invasion under various drilling fluid salinity values.

#### 4. Conclusions

A two-dimensional numerical model was established to simulate the drilling process in the reservoir. Aiming at the hydrate reservoir at station W17 in the Shenhu area of the South China Sea, the physical response characteristics of the reservoir during the drilling process were simulated and analyzed. The effects of the drilling fluid temperature and salinity were studied. The following conclusions are drawn:

- (1) During the process of drilling in the reservoir, the temperature and pressure of the reservoir respond quickly in a large area, which accelerates the decomposition of the hydrate in the reservoir around the wellbore. The decomposition process delays the heat transfer of the reservoir and generates a large amount of gas and water, leading

to secondary hydrate formation. A high hydrate saturation zone appears near the hydrate decomposed in the layer without free gas, which corresponds to the low water saturation and high salinity zone. The hydrate decomposition area of the layer with free gas is larger than that of the layer without free gas.

- (2) The increase in the drilling fluid temperature can significantly enhance the hydrate decomposition of both layers in the reservoir. Hydrate decomposition near the wellbore under a high drilling fluid temperature will cause a sharp increase in the pressure in the reservoir, leading to the flow of pore fluid into the wellbore. The heat conduction from the wellbore to the reservoir is the main factor influencing hydrate decomposition in the reservoir at a high drilling fluid temperature under the simulation conditions in this study.
- (3) With the increase in drilling fluid salinity, the extent of hydrate decomposition in the reservoir is little affected. When the salinity exceeds 10%wt, the range of hydrate decomposition has almost no changes. However, the salinity of the pore water in the layer with free gas is obviously increased.
- (4) The amount of the drilling fluid invasion is one of the response characteristics of the reservoir. With the increase in drilling fluid salinity, the invasion amount of drilling fluid decreases gradually. As the drilling fluid temperature increases, the possibility of the fluid in pores in the reservoir flowing into the wellbore and the gas invasion will be greatly increased in the early stage. It is critically important to control the drilling fluid temperature in the early stage to prevent the invasion of gas from the reservoir to the wellbore.

This study is mainly aimed at natural gas hydrate reservoirs with low permeability in the South China Sea. The simulation calculation results in this study can be applied to other natural gas hydrate reservoirs with similar conditions in the world, such as the eastern enrichment area of the hydrate layer in the Nankai Trough of Japan [31] and the natural gas hydrate reservoir on the continental margin of India [32], aiding in the interpretation of drilling behaviors and the optimization of drilling operations in the hydrate layer.

**Author Contributions:** Conceptualization, L.Z. and Y.Z.; methodology, Y.Z.; software, L.Z. and Y.Z.; investigation, L.Z. and C.C.; writing—original draft preparation, L.Z.; writing—review and editing, Y.Z. and C.C.; supervision, X.-S.L. and Z.-Y.C.; funding acquisition, X.-S.L. All authors have read and agreed to the published version of the manuscript.

**Funding:** This work was funded by the National Natural Science Foundation of China (52076208, 51736009), the Guangdong Special Support Program (2019BT02L278), and the Special Project for Marine Economy Development of Guangdong Province (GDME-2020D044), which are gratefully acknowledged.

**Data Availability Statement:** Not applicable.

**Conflicts of Interest:** The authors declare no conflict of interest. The funders had no role in study design; data collection, analysis, and interpretation; manuscript writing; or decision to publish results.

## Appendix A

Discretization of mass conservation equation:

The Darcy seepage velocity equation is brought into the original mass conservation equation:

Gas-phase mass conservation equation:

$$\frac{\partial(\phi\rho_g S_g)}{\partial t} = \frac{1}{r} \frac{\partial}{\partial r} \left( r\rho_g \frac{KK_g}{\mu_g} \frac{\partial P_g}{\partial r} \right) + \frac{\partial}{\partial z} \left( \rho_g \frac{KK_g}{\mu_g} \frac{\partial (P_g - \gamma_{gz}g\Delta z)}{\partial z} \right) + m_g M_g \quad (\text{A1})$$

Liquid-phase mass conservation equation:

$$\frac{\partial(\phi\rho_w S_w)}{\partial t} = \frac{1}{r} \frac{\partial}{\partial r} \left( r\rho_w \frac{KK_w}{\mu_w} \frac{\partial P_w}{\partial r} \right) + \frac{\partial}{\partial z} \left( \rho_w \frac{KK_w}{\mu_w} \frac{\partial (P_w - \gamma_{wz}g\Delta z)}{\partial z} \right) + m_w M_w \quad (\text{A2})$$

Hydrate-phase mass conservation equation:

$$\frac{\partial(\varphi\rho_h S_h)}{\partial t} = -\dot{m}_h(M_g + n_w M_w) \quad (A3)$$

The implicit central difference scheme is used for finite difference discretization on the right ends of the above formulas. In the time discretization, the backward Euler method is used to discretize the non-stationary term and the difference format which is obtained by taking the calculation of the middle point of the uppermost layer for an example. In the difference equation, the subscript “*i*” and superscript “*n + 1*” of pressure and saturation terms are omitted.

Gas phase:

$$\left(\frac{K_r K_{rg}}{\mu_g}\right)_{i-1} \frac{(P_{g(i-1)} - P_g)}{\Delta r} r_{i-0.5} \rho_{g(i-1)} \Delta z - \frac{K_r K_{rg}}{\mu_g} \frac{(P_g - P_{g(i+1)})}{\Delta r_{i+1}} r_{i+0.5} \rho_g \Delta z - \left(\frac{K_r K_{rg}}{\mu_g}\right)_{i+N_x} \frac{(P_g - P_{g(i+N_x)})}{\Delta z} r \frac{\Delta r + \Delta r_{i+1}}{2} \rho_{g(i+N_x)} - \left(\frac{K_r K_{rg}}{\mu_g}\right)_{i+N_x} r \frac{\Delta r + \Delta r_{i+1}}{2} \rho_g \Delta z \times 10^{-6} + r \frac{\Delta r + \Delta r_{i+1}}{2} \dot{m}_g M_g \Delta z = \varphi r \frac{\Delta r + \Delta r_{i+1}}{2} \Delta z \left(\rho_g \frac{S_g - S_g^n}{\Delta t} + S_g \rho_g (C_{pg} + C_{pr} / \varphi) \frac{P_g - P_g^n}{\Delta t}\right) \quad (A4)$$

Liquid phase:

$$\left(\frac{K_r K_{rw}}{\mu_w}\right)_{i-1} \frac{(P_{w(i-1)} - P_w)}{\Delta r} r_{i-0.5} \rho_{w(i-1)} \Delta z - \frac{K_r K_{rw}}{\mu_w} \frac{(P_w - P_{w(i+1)})}{\Delta r_{i+1}} r_{i+0.5} \rho_w \Delta z - \left(\frac{K_r K_{rw}}{\mu_w}\right)_{i+N_x} \frac{(P_w - P_{w(i+N_x)})}{\Delta z} r \frac{\Delta r + \Delta r_{i+1}}{2} \rho_{w(i+N_x)} - \left(\frac{K_r K_{rw}}{\mu_w}\right)_{i+N_x} r \frac{\Delta r + \Delta r_{i+1}}{2} \rho_w \Delta z \times 10^{-6} + r \frac{\Delta r + \Delta r_{i+1}}{2} \dot{m}_w M_w \Delta z = \varphi r \frac{\Delta r + \Delta r_{i+1}}{2} \Delta z \left(\rho_w \frac{S_w - S_w^n}{\Delta t} + S_w \rho_w (C_{pw} + C_{pr} / \varphi) \frac{P_w - P_w^n}{\Delta t}\right) \quad (A5)$$

Hydrate phase:

$$\varphi r \frac{\Delta r + \Delta r_{i+1}}{2} \rho_h \frac{S_h - S_h^n}{\Delta t} = -r \frac{\Delta r + \Delta r_{i+1}}{2} \dot{m}_h (M_g + n_w M_w) \quad (A6)$$

The Darcy seepage velocity equation is brought into the original mass conservation equation in the same way:

$$\frac{1}{r} \frac{\partial}{\partial r} \left( r \lambda_c \frac{\partial T}{\partial r} \right) + \frac{\partial}{\partial z} \left( \lambda_c \frac{\partial T}{\partial z} \right) + \frac{\partial}{\partial r} \left\{ r \left( \rho_g C_g T \frac{K K_g}{\mu_g} \frac{\partial P_g}{\partial r} + \rho_w C_w T \frac{K K_w}{\mu_w} \frac{\partial P_w}{\partial r} \right) \right\} + \frac{\partial}{\partial z} \left( \rho_g C_g T \frac{K K_g}{\mu_g} \frac{\partial (P_g - \gamma_{gz} \Delta z)}{\partial z} + \rho_w C_w T \frac{K K_w}{\mu_w} \frac{\partial (P_w - \gamma_{wz} \Delta z)}{\partial z} \right) - \dot{m}_h \Delta H = \frac{\partial(TC_h)}{\partial t} \quad (A7)$$

The finite difference scheme of the energy conservation equation is implemented as follows, where the heat conduction term is discretized by the display center difference scheme and the convection term is discretized by the explicit upwind scheme [33]:

Discretization of mass conservation equation of salinity:

$$\left( \lambda_{i-0.5} r_{i-0.5} \frac{(T_{i-1} - T)}{\Delta r} - \lambda_{i+0.5} r_{i+0.5} \frac{(T - T_{i+1})}{\Delta r} \right) \Delta z + \left\{ \rho_g C_g \left( \frac{K_r K_{rg}}{\mu_g} \right)_{i-1} \frac{(P_{g(i-1)} - P_g)}{\Delta r} + \rho_w C_w \left( \frac{K_r K_{rw}}{\mu_w} \right)_{i-1} \frac{(P_{w(i-1)} - P_w)}{\Delta r} \right\} r_{i-0.5} \Delta z T_{i-1} - \left\{ \rho_g C_g \frac{K_r K_{rg}}{\mu_g} \frac{(P_g - P_{g(i+1)})}{\Delta r_{i+1}} + \rho_w C_w \frac{K_r K_{rw}}{\mu_w} \frac{(P_w - P_{w(i+1)})}{\Delta r_{i+1}} \right\} r_{i+0.5} \Delta z T_i - \lambda r \frac{\Delta r + \Delta r_{i+1}}{2} \frac{(T_i - T_{i+N_x})}{\Delta z} - \left( \rho_g (i+N_x) C_g \left( \frac{K_r K_{rg}}{\mu_g} \right)_{(i+N_x)} \frac{(P_g - P_{g(i+N_x)})}{\Delta r} + \rho_w (i+N_x) C_w \left( \frac{K_r K_{rw}}{\mu_w} \right)_{(i+N_x)} \frac{(P_w - P_{w(i+N_x)})}{\Delta r} \right) \frac{\Delta r + \Delta r_{i+1}}{2} \frac{r}{\Delta z} - r \frac{\Delta r + \Delta r_{i+1}}{2} \dot{m}_h (M_g + n_w M_w) \Delta H = r \frac{\Delta r + \Delta r_{i+1}}{2} \frac{C_i T - (C_i T)^n}{\Delta t} \quad (A8)$$

The Darcy seepage velocity equation is brought into the original salinity mass conservation equation in the same way:

$$\frac{\partial(\varphi \rho_w S_w X_s)}{\partial t} = \frac{1}{r} \frac{\partial}{\partial r} \left( r \rho_w X_s \frac{K K_w}{\mu_w} \frac{\partial P_w}{\partial r} \right) + \frac{\partial}{\partial z} \left( \rho_w X_s \frac{K K_w}{\mu_w} \frac{\partial P_w}{\partial z} \right) + k_D \left\{ \frac{1}{r} \frac{\partial}{\partial r} \left( \varphi r \rho_w S_w \frac{\partial X_s}{\partial r} \right) + \frac{\partial}{\partial z} \left( \varphi \rho_w S_w \frac{\partial X_s}{\partial z} \right) \right\} \quad (A9)$$

The finite difference scheme of the salinity mass conservation equation is as follows:

$$\left(\frac{K_r K_{rw}}{\mu_w}\right)_{i-1} \frac{(P_{w(i-1)} - P_w)}{\Delta r} r_{i-0.5} \Delta z (X_{s(i-1)})^n - \frac{K_r K_{rw}}{\mu_w} \frac{(P_w - P_{w(i+1)})}{\Delta r_{i+1}} r_{i+0.5} \Delta z (X_{s(i)})^n - \left(\frac{K_r K_{rw}}{\mu_w}\right)_{i+N_x} \frac{(P_w - P_{w(i+N_x)})}{\Delta z} r \frac{\Delta r + \Delta r_{i+1}}{2} (X_{s(i+N_x)})^n - \left(\frac{K_r K_{rw}}{\mu_w}\right)_{i-N_x} \frac{(P_w - P_{w(i-N_x)})}{\Delta z} r \frac{\Delta r + \Delta r_{i+1}}{2} (X_{s(i-N_x)})^n + r \Delta z (\varphi_{(i-1)})^n (S_{w(i-1)})^n K_{DD} \frac{(X_{s(i-1)} - X_s)}{\Delta r_i} - r \Delta z (\varphi_{(i)})^n (S_w)^n K_{DD} \frac{(X_s - X_{s(i+1)})}{\Delta r_{i+1}} - r \frac{\Delta r + \Delta r_{i+1}}{2} (\varphi_{(i-N_x)})^n (S_{w(i-N_x)})^n K_{DD} \frac{(X_s - X_{s(i-N_x)})}{\Delta z} - r \frac{\Delta r + \Delta r_{i+1}}{2} (\varphi_{(i+N_x)})^n (S_{w(i+N_x)})^n K_{DD} \frac{(X_s - X_{s(i+N_x)})}{\Delta z} = r \frac{\Delta r + \Delta r_{i+1}}{2} \Delta z \frac{X_s \varphi S_w - (X_s \varphi S_w)^n}{\Delta t} \quad (A10)$$

The detailed solution process of the discrete equation is as follows:

- (1) Firstly, the natural gas hydrate kinetic equation is solved according to the divided elements and relevant basic parameters to obtain the hydrate decomposition or generation amount at the initial moment (determined by the phase equilibrium state at the moment), so as to calculate the hydrate saturation at the next moment:

$$S_h = S_h^n - \dot{m}_h \frac{\Delta t}{\varphi \rho_h} \quad (\text{A11})$$

- (2) By combining Equations (A4)–(A6), the saturation equation, and the capillary pressure equation, the pressure of the hydrate reservoir for the next moment is obtained and solved by the LU decomposition method [22]:

$$\begin{aligned} & \left( \frac{K_r K_{rw}}{\mu_w} \right)_{i-1} \frac{(P_w(i-1) - P_w)}{\Delta r} \Delta z r_{i-0.5} \frac{\rho_w(i-1)}{\rho_w} - \frac{K_r K_{rw}}{\mu_w} \frac{(P_w - P_w(i+1))}{\Delta r_{i+1}} \Delta z r_{i+0.5} - \left( \frac{K_r K_{rw}}{\mu_w} \right)_{i+Nx} \frac{(P_w - P_w(i+Nx))}{\Delta z} r \frac{\Delta r + \Delta r_{i+1}}{2} \frac{\rho_w(i+Nx)}{\rho_w} \\ & - \left( \frac{K_r K_{rw}}{\mu_w} \right)_{i+Nx} r \frac{\Delta r + \Delta r_{i+1}}{2} \Delta z G * 10^{-6} + \left( \frac{K_r K_{rg}}{\mu_g} \right)_{i-1} \frac{(P_g(i-1) - P_g)}{\Delta r} \Delta z r_{i-0.5} \frac{\rho_g(i-1)}{\rho_g} - \frac{K_r K_{rg}}{\mu_g} \frac{(P_g - P_g(i+1))}{\Delta r_{i+1}} \Delta z r_{i+0.5} \\ & - \left( \frac{K_r K_{rg}}{\mu_g} \right)_{i+Nx} \frac{(P_g - P_g(i+Nx))}{\Delta z} r \frac{\Delta r + \Delta r_{i+1}}{2} \frac{\rho_g(i+Nx)}{\rho_g} \\ & - \left( \frac{K_r K_{rg}}{\mu_g} \right)_{i+Nx} r \frac{\Delta r + \Delta r_{i+1}}{2} \Delta z g \times 10^{-6} + r \frac{\Delta r + \Delta r_{i+1}}{2} \dot{m}_w \frac{M_w}{\rho_w} + r \frac{\Delta r + \Delta r_{i+1}}{2} \dot{m}_g \frac{M_g}{\rho_g} - r \frac{\Delta r + \Delta r_{i+1}}{2} \frac{M_h}{\rho_h} \\ & = \varphi r \frac{\Delta r + \Delta r_{i+1}}{2} \left( S_w^n (C_{pw} + C_{pr}/\varphi) \frac{P_w - P_w^n}{\Delta t} + S_g^n (C_{pg} + C_{pr}/\varphi) \frac{P_g - P_g^n}{\Delta t} \right) \end{aligned} \quad (\text{A12})$$

- (3) The water saturation of the reservoir is obtained by solving the water saturation mass conservation equation according to the known pressure distribution at the next moment:

$$S_w = \left[ \begin{aligned} & S_w^n \varphi_{old} + \Delta t \left( \left( \frac{K_r K_{rw}}{\mu_w} \right)_{i-1} \frac{(P_w(i-1) - P_w)}{\Delta r} r_{i-0.5} \frac{\rho_w(i-1)}{\rho_w} \Delta z - \frac{K_r K_{rw}}{\mu_w} \frac{(P_w - P_w(i+1))}{\Delta r_{i+1}} r_{i+0.5} \Delta z - \left( \frac{K_r K_{rw}}{\mu_w} \right)_{i+Nx} \frac{(P_w - P_w(i+Nx))}{\Delta z} r \frac{\Delta r + \Delta r_{i+1}}{2} \frac{\rho_w(i+Nx)}{\rho_w} \right. \\ & \left. - \left( \frac{K_r K_{rw}}{\mu_w} \right)_{i+Nx} r \frac{\Delta r + \Delta r_{i+1}}{2} \Delta z g \times 10^{-6} + r \frac{\Delta r + \Delta r_{i+1}}{2} \dot{m}_w \frac{M_w}{\rho_w} \Delta z \right) \\ & \div \left( \varphi r \frac{\Delta r + \Delta r_{i+1}}{2} \Delta z \right) \\ & \div \left( (C_{pw} + C_{pr}/\varphi) \frac{P_w - P_w^n}{\Delta t} \varphi \right) \end{aligned} \right] \quad (\text{A13})$$

- (4) The salinity distribution of the hydrate reservoir is obtained by solving Equation (29) according to the pressure of the reservoir and the saturation distribution of each phase obtained in the previous section:

$$X_s = \frac{\left[ \begin{aligned} & \left( \frac{K_r K_{rw}}{\mu_w} \right)_{i-1} \frac{(P_w(i-1) - P_w)}{\Delta r} r_{i-0.5} \Delta z (x_{(i-1)})^n - \frac{K_r K_{rw}}{\mu_w} \frac{(P_w - P_w(i+1))}{\Delta r_{i+1}} r_{i+0.5} \Delta z (x_{(i)})^n - \left( \frac{K_r K_{rw}}{\mu_w} \right)_{i+Nx} \frac{(P_w - P_w(i+Nx))}{\Delta z} r \frac{\Delta r + \Delta r_{i+1}}{2} (x_{(i+Nx)})^n \\ & - \left( \frac{K_r K_{rw}}{\mu_w} \right)_{i+Nx} \frac{(P_w - P_w(i+Nx))}{\Delta z} r \frac{\Delta r + \Delta r_{i+1}}{2} (x_{(i-Nx)})^n + r \Delta z (\varphi_{(i-1)})^n (S_w(i-1))^n K_{DD} \frac{(X_s(i-1) - X_s)}{\Delta r_i} - r \Delta z (\varphi_{(i)})^n (S_w)^n K_{DD} \frac{(X_s - X_s(i+1))}{\Delta r_{i+1}} \\ & - r \frac{\Delta r + \Delta r_{i+1}}{2} (\varphi_{(i-Nx)})^n (S_w(i-Nx))^n K_{DD} \frac{(X_s - X_s(i-Nx))}{\Delta z} - r \frac{\Delta r + \Delta r_{i+1}}{2} (\varphi_{(i+Nx)})^n (S_w(i+Nx))^n K_{DD} \frac{(X_s - X_s(i+Nx))}{\Delta z} \\ & + r \frac{\Delta r + \Delta r_{i+1}}{2} \Delta z (X_s \varphi S_w)^n \end{aligned} \right]}{r \frac{\Delta r + \Delta r_{i+1}}{2} \Delta z \varphi S_w} \quad (\text{A14})$$

- (5) Finally, the energy conservation equation is solved by the LU decomposition method again to obtain the temperature distribution of the reservoir:

$$\begin{aligned} & \left( \lambda_{i-0.5} r_{i-0.5} \frac{(T_{i-1} - T)}{\Delta r} - \lambda_{i+0.5} r_{i+0.5} \frac{(T - T_{i+1})}{\Delta r} \right) \Delta z + \left\{ \rho_g C_g \left( \frac{K_r K_{rg}}{\mu_g} \right)_{i-1} \frac{(P_g(i-1) - P_g)}{\Delta r} + \rho_w C_w \left( \frac{K_w K_{rw}}{\mu_w} \right)_{i-1} \frac{(P_w(i-1) - P_w)}{\Delta r} \right\} r_{i-0.5} \Delta z T \\ & - \left\{ \rho_g C_g \frac{K_r K_{rg}}{\mu_g} \frac{(P_g - P_g(i+1))}{\Delta r_{i+1}} + \rho_w C_w \frac{K_w K_{rw}}{\mu_w} \frac{(P_w - P_w(i+1))}{\Delta r_{i+1}} \right\} r_{i+0.5} \Delta z T_i - \lambda r \frac{\Delta r + \Delta r_{i+1}}{2} \frac{(T_i - T_{i+Nx})}{\Delta z} \\ & - \left( \rho_g(i+Nx) C_g \left( \frac{K_r K_{rg}}{\mu_g} \right)_{(i+Nx)} \frac{(P_g - P_g(i+Nx))}{\Delta r} + \rho_w(i+Nx) C_w \left( \frac{K_w K_{rw}}{\mu_w} \right)_{(i+Nx)} \frac{(P_w - P_w(i+Nx))}{\Delta r} \right) \frac{\Delta r + \Delta r_{i+1}}{2} \frac{r}{\Delta z} \\ & - r \frac{\Delta r + \Delta r_{i+1}}{2} \dot{m}_h (M_g + n_w M_w) \Delta H = r \frac{\Delta r + \Delta r_{i+1}}{2} C_t T - (C_t T)^n \end{aligned} \quad (\text{A15})$$

All parameters (including temperature, pressure, phase saturation, and salinity) of the solution results are updated as the initial conditions for the next time step to calculate the

temperature, pressure, salinity, saturation, etc., in each time step distributed until the set calculation time is completed.

## Appendix B

As shown in Figure A1, the pressure and temperature distribution curves at 25 m from the bottom of the reservoir in the simulation results with the lateral element spacing parameter values of 0.01 m, 0.015 m, 0.02 m, 0.03 m, 0.05 m, and 0.1 m are compared. The closer the lateral element spacing parameter is to 0.01 m, the closer the pressure and temperature distributions of the numerical simulation results are. It can be proved that the lateral element spacing parameter selected in this model as 0.01 m is reasonable.

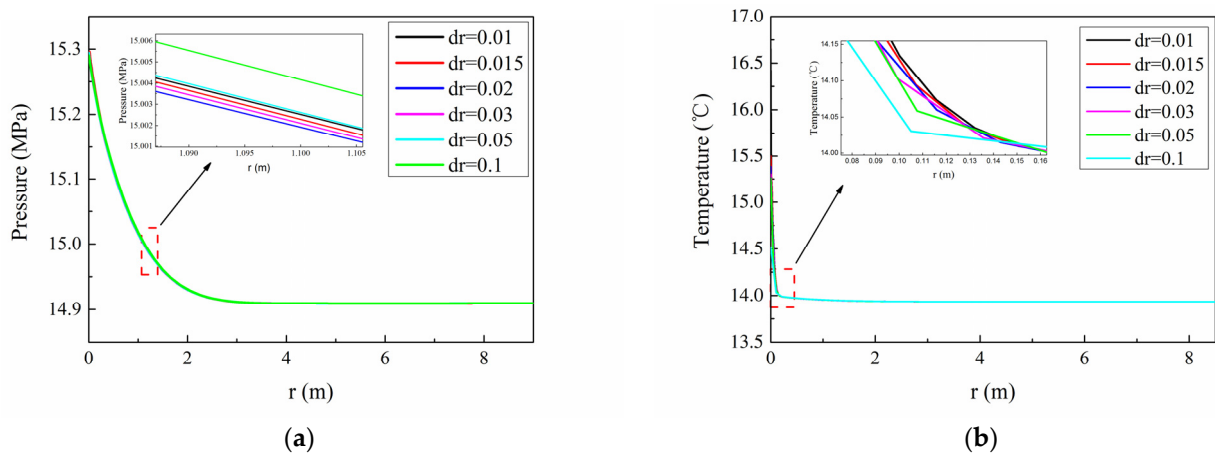


**Figure A1.** Comparison of the pressure and temperature distribution curves at 25 m from the bottom of the reservoir in the simulation results with lateral element spacing parameter values of 0.01 m, 0.015 m, 0.02 m, 0.03 m, and 0.05 m: (a) pressure distribution; (b) temperature distribution.

Figure A2 presents a comparison of the pressure and temperature distribution curves at 25 m from the bottom of the reservoir in the simulation results with the vertical element spacing values of 1 m, 2 m, 3 m, and 5 m. As shown in Figure A2, the simulation results for different vertical element spacing values are basically the same, and the pressure and temperature curves overlap. The closer the vertical element spacing parameter is to 1 m, the closer the temperature distribution of the numerical simulation results is. It can be proved that the vertical element spacing selected in this model as 1 m is reasonable.

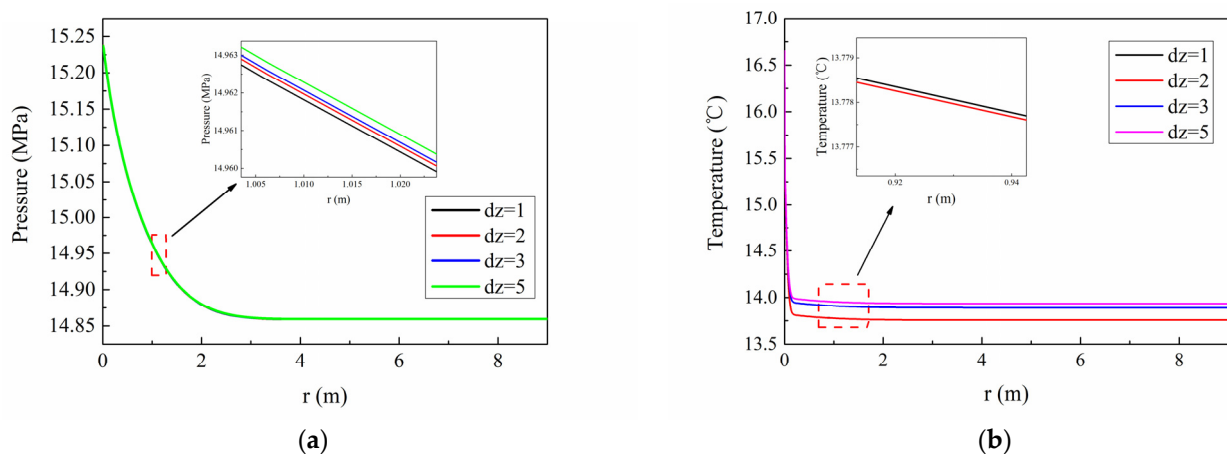


**Figure A2.** Comparison of the pressure and temperature distribution curves at 25 m from the bottom of the reservoir in the simulation results with vertical element spacing parameter values of 1 m, 2 m, 3 m, and 5 m: (a) pressure distribution; (b) temperature distribution.

## References

1. Blank, L.; Rioseco, E.M.; Caiazzo, A.; Wilbrandt, U. Modeling, simulation, and optimization of geothermal energy production from hot sedimentary aquifers. *Comput. Geosci.* **2021**, *25*, 67–104. [[CrossRef](#)]
2. Lee, S.Y.; Holder, G.D. Methane hydrates potential as a future energy source. *Fuel Process. Technol.* **2001**, *71*, 181–186. [[CrossRef](#)]
3. Sloan, E.D.J.; Koh, C.A. *Clathrate Hydrates of Natural Gases*, 3rd ed.; Taylor & Francis Group: Boca Raton, FL, USA, 2008.
4. Demirbas, A. Methane hydrates as potential energy resource: Part 1-Importance, resource and recovery facilities. *Energy Convers. Manag.* **2010**, *51*, 1547–1561. [[CrossRef](#)]
5. Klauda, J.B.; Sandler, S.I. Global distribution of methane hydrate in ocean sediment. *Energy Fuels* **2005**, *19*, 459–470. [[CrossRef](#)]
6. Milkov, A.V.; Sassen, R.; Novikova, I.; Mikhailov, E. Gas Hydrates at Minimum Stability Water Depths in the Gulf of Mexico: Significance to Geohazard Assessment. *Gcags Trans.* **2000**, *45*, 217–224.
7. Campbell, K.J. Deep water geohazards: How significant are they? *Lead. Edge* **1999**, *18*, 514–519. [[CrossRef](#)]
8. Lee, M.W. Elastic velocities of partially gas-saturated unconsolidated sediments. *Mar. Pet. Geol.* **2004**, *21*, 641–650. [[CrossRef](#)]
9. Chong, Z.R.; Yang, S.H.B.; Babu, P.; Linga, P.; Li, X.S. Review of natural gas hydrates as an energy resource: Prospects and challenges. *Appl. Energy* **2016**, *162*, 1633–1652. [[CrossRef](#)]
10. Zhang, H.; Cheng, Y.; Li, Q.; Yan, C.; Han, X. Numerical analysis of wellbore instability in gas hydrate formation during deep-water drilling. *J. Ocean Univ. China* **2018**, *17*, 8–16. [[CrossRef](#)]
11. Yun, T.S.; Santamarina, J.C.; Ruppel, C. Mechanical properties of sand, silt, and clay containing tetrahydrofuran hydrate. *J. Geophys. Res. Solid Earth* **2007**, *112*. [[CrossRef](#)]
12. Ning, F.L.; Zhang, K.N.; Wu, N.Y.; Jiang, G.S.; Zhang, L.; Liu, L.; Yu, Y.B. Invasion of water-based drilling mud into oceanic gas-hydrate-bearing sediment: One-dimensional numerical simulations. *Chin. J. Geophys.-Chin.* **2013**, *56*, 204–218.
13. Moridis, G.J.; Kowalsky, M.; Max, M.; Johnson, A.H.; Dillon, W.P. Gas Production from Unconfined Class 2 Oceanic Hydrate Accumulations. In *Economic Geology of Natural Gas Hydrate*; Haq, B.U., Ed.; Springer: Dordrecht, The Netherlands, 2006; pp. 249–266.
14. Birchwood, R.; Noeth, S.; Tjengdrawira, M.; Kusra, S.; Bloys, J. In Modeling the Mechanical and Phase Change Stability of Wellbores Drilled in Gas Hydrates by the Joint Industry Participation Program (JIP) Gas Hydrates Project, Phase II. In Proceedings of the SPE Annual Technical Conference and Exhibition, Anaheim, CA, USA, 11–14 November 2007.
15. Botrel, T. Hydrates Prevention and Removal in Ultra-Deepwater Drilling Systems. *Polym. Test.* **2001**, *27*, 841–850.
16. Paull, C.K.; Matsumoto, R.; Wallace, P.J. *Proceedings, Initial Reports, Ocean Drilling Program, Leg 164, Gas Hydrate Sampling on the Blake Ridge and Carolina Rise*; ODP, Texas A & M University: College Station, TX, USA, 1996.
17. Gao, Y.; Sun, B.; Xu, B.; Wu, X.; Chen, Y.; Zhao, X.; Chen, L. A Wellbore/Formation-Coupled Heat-Transfer Model in Deepwater Drilling and Its Application in the Prediction of Hydrate-Reservoir Dissociation. *SPE J.* **2017**, *22*, 756–766. [[CrossRef](#)]
18. Freij-Ayoub, R.; Tan, C.; Clennell, B.; Tohidi, B.; Yang, J. A wellbore stability model for hydrate bearing sediments. *J. Pet. Sci. Eng.* **2007**, *57*, 209–220. [[CrossRef](#)]
19. Cheng, Y.F.; Li, L.D.; Mahmood, S.; Cui, Q. Fluid-solid coupling model for studying wellbore instability in drilling of gas hydrate bearing sediments. *Appl. Math Mech.-Engl.* **2013**, *34*, 1421–1432. [[CrossRef](#)]
20. Sun, J.; Ning, F.; Lei, H.; Gai, X.; Sanchez, M.; Lu, J.; Li, Y.; Liu, L.; Liu, C.; Wu, N.; et al. Wellbore stability analysis during drilling through marine gas hydrate-bearing sediments in Shenhu area: A case study. *J. Pet. Sci. Eng.* **2018**, *170*, 345–367. [[CrossRef](#)]
21. Li, Q.; Liu, L.; Yu, B.; Guo, L.; Shi, S.; Miao, L. Borehole enlargement rate as a measure of borehole instability in hydrate reservoir and its relationship with drilling mud density. *J. Pet. Explor. Prod.* **2021**, *11*, 1185–1198. [[CrossRef](#)]
22. Yu, L.; Xu, Y.; Gong, Z.; Huang, F.; Zhang, L.; Ren, S. Experimental study and numerical modeling of methane hydrate dissociation and gas invasion during drilling through hydrate bearing formations. *J. Pet. Sci. Eng.* **2018**, *168*, 507–520. [[CrossRef](#)]
23. Huang, T.J.; Zhang, Y.; Li, G.; Li, X.S.; Chen, Z.Y. Numerical modeling for drilling fluid invasion into hydrate-bearing sediments and effects of permeability. *J. Pet. Sci. Eng.* **2020**, *77*, 103239. [[CrossRef](#)]
24. Moridis, G.J.; Kowalsky, M.B.; Pruess, K. Depressurization-Induced Gas Production from Class-1 Hydrate Deposits. *SPE Reserv. Eval. Eng.* **2007**, *10*, 458–481. [[CrossRef](#)]
25. Li, J.F.; Ye, J.L.; Qin, X.W.; Qiu, H.J.; Wu, N.Y.; Lu, H.L.; Xie, W.W.; Lu, J.A.; Peng, F.; Xu, Z.Q. The first offshore natural gas hydrate production test in South China Sea. *China Geol.* **2018**, *1*, 5–16. [[CrossRef](#)]
26. Kim, H.C.; Bishnoi, P.R.; Heidemann, R.A.; Rizvi, S. Kinetics of methane hydrate decomposition. *Chem. Eng. Sci.* **1987**, *42*, 1645–1653. [[CrossRef](#)]
27. Malegaonkar, M.B.; Dholabhai, P.D.; Bishnoi, P.R. Kinetics of carbon dioxide and methane hydrate formation. *Can. J. Chem. Eng.* **1997**, *75*, 1090–1099. [[CrossRef](#)]
28. Li, C.; Zhao, Q.; Xu, H.; Feng, K.; Liu, X. Relation between relative permeability and hydrate saturation in Shenhu area, South China Sea. *Appl. Geophys.* **2014**, *11*, 207–214. [[CrossRef](#)]
29. Stone, H.L. Probability Model for Estimating Three-Phase Relative Permeability. *J. Pet. Technol.* **1970**, *22*, 214–218. [[CrossRef](#)]
30. McConnell, D.R.; Zhang, Z.; Boswell, R. Review of progress in evaluating gas hydrate drilling hazards. *Mar. Pet. Geol.* **2012**, *34*, 209–223. [[CrossRef](#)]
31. Uchida, T.; Tsuji, T. Petrophysical properties of natural gas hydrates-bearing sands and their sedimentology in the Nankai Trough. *Resour. Geol.* **2004**, *54*, 79–87. [[CrossRef](#)]

32. Singh, R.P.; Lall, D.; Vishal, V. Prospects and challenges in unlocking natural-gas-hydrate energy in India: Recent advancements. *Mar. Pet. Geol.* **2022**, *135*, 105397. [[CrossRef](#)]
33. Wang, X.R.; Sun, B.J.; Gao, Y.H.; Wang, Z.Y.; Li, H.; Chen, Y. Numerical simulation of the stability of hydrate layer during well cementing in deep-water region. *J. Pet. Sci. Eng.* **2019**, *176*, 893–905. [[CrossRef](#)]